

Dose enhancement in bone and in tissue due to photonuclear  
disintegration processes

A DISSERTATION  
SUBMITTED TO THE FACULTY OF  
UNIVERSITY OF MINNESOTA  
BY

Pamela Sooriyan

IN PARTIAL FULFILLMENT OF THE REQUIREMENTS  
FOR THE DEGREE OF  
DOCTOR OF PHILOSOPHY

John Broadhurst, Ph.D., Adviser

March 2017

© Pamela Sooriyan 2017

## Acknowledgements

I am grateful to several individuals who generously gave their time and expertise during the last several years.

First and foremost, I would like to thank my adviser, Dr. John Broadhurst. He has been very generous in sharing his extraordinary scope of knowledge and offering help and advice with the experiments. He has been patient in responding to questions, and generous in offering his input into my work and my writing.

I would also like to thank Dr. Benjamin Bayman, who was always willing to offer help especially with mathematical derivations. He has also been kind and patient in responding to questions, offering explanations, and providing feedback for my writing.

I specially thank Dr. Bruce Gerbi for providing me with access to the linear accelerator and for his valuable feedback for my writing. Dr. Patrick Higgins was very helpful in giving me access to the linear accelerator, teaching me and trusting me with operating the linear accelerator.

Finally, I would like to thank my friend Sara Simmers for her friendship and consistent support through these arduous years.

Minnesota  
January 27, 2017

*Pamela Sooriyan*

This thesis is dedicated to  
my parents, Mr. and Mrs. Sooriyan

# Contents

Table of Contents .....	iii
List of Tables .....	vi
List of figures.....	vii

## Table of Contents

### Chapter 1 Introduction

1.1 Available treatments options using photons and their interaction processes ....	1
1.1.1 Photoelectric absorption .....	2
1.1.2 Compton scattering .....	4
1.1.3 Pair production .....	5
1.1.4 Photo disintegration .....	7
( $\gamma,n$ ) reactions .....	8
$^{16}\text{O}(\gamma,n)^{15}\text{O}$ reaction .....	9
$^{12}\text{C}(\gamma,n)^{11}\text{C}$ reaction .....	13
Giant dipole resonance .....	13
1.2 Doping techniques .....	16
1.2.1 Neutron Capture therapy .....	16
Boron neutron capture therapy .....	17
Gadolinium neutron capture therapy .....	18
1.2.2 Enhancing dose by introducing high atomic number material in the treatment region .....	18
Dose enhancement by photo electric absorption .....	19
Dose enhancement by pair production .....	20
1.2.3 Tumor-targeting radiopharmaceuticals .....	20
Metabolic radiation therapy .....	21
1.3 Advantages of local dose enhancement in external beam radiation therapy.....	21

## **Chapter 2 Experiment**

2.1	Proposed procedure for the experiment .....	24
2.1.1	Filter to absorb the lower end of Bremsstrahlung .....	25
2.1.2	Output of the linear accelerator .....	26
	Signals observed .....	26
	Observing the signals using an operational amplifier as a virtual ground .....	29
2.1.3	Design of the radiation time monitor .....	32
2.2	The experiment .....	36
2.2.1	Calibrating the multi-channel analyser .....	37
2.2.2	The detector .....	41
	Measured detector parameter .....	42
2.2.3	Calibrating the detector .....	44
2.2.4	Sample to be irradiated .....	45
2.2.5	The various trials .....	45
2.3	The modified procedure .....	47
2.3.1	Trial 1 .....	49
2.3.2	Trial 2 .....	50

## **Chapter 3 Analysis and results**

3.1	Analysis of data .....	51
3.2	Result .....	60

## **Chapter 4 Discussion**

4.1	Energy of the incident photons .....	62
4.2	Interaction cross-section for the observed reaction .....	64

4.3	Dose due to positrons released .....	64
4.3.1	The range of the positrons .....	65
4.3.2	Linear energy transfer of the positrons .....	67
4.3.3	Measured local dose enhancement due to positrons .....	68
4.4	Thermoluminescent dosimeters .....	70
<b>Chapter 5 Conclusion</b>		
5.1	Measured local dose enhancement from the spectra .....	71
5.1.1	Expected positron yield .....	71
5.2	Enhancing the reaction in a high energy linear accelerator .....	72
5.2.1	Filter to absorb the lower end of bremsstrahlung .....	73
5.2.2	Neutron contamination .....	74
5.3	Enhancing the reaction by quasi mono energetic beams.....	75
5.3.1	Annihilation in flight of mono energetic fast positrons .....	75
5.4	Conclusion .....	76
	References .....	77
	Appendix 1 .....	83
	Appendix 2 .....	84
	Appendix 3 .....	85

## List of tables

<b>Table 2.1</b> Present activity, half-life, energy and emission probability of the isotopes used for calibration .....	33
<b>Table 2.2</b> Peak to Compton ratio obtained with the NaI detector .....	38
<b>Table 2.3</b> Relative resolution and resolution efficiency of the detector .....	39



## List of figures

<b>Figure 1-1</b> Mass attenuation coefficient ( $\tau/\rho$ ) vs. photon energy curves for water ( $Z_{\text{eff}} = 7.42$ ) and for lead ( $Z = 82$ ) .....	3
<b>Figure 1-2</b> Compton scattering .....	4
<b>Figure 1-3</b> Pair production .....	6
<b>Figure 1-4</b> Total photon cross section $\sigma_{\text{tot}}$ in tissue, as a function of photon energy, showing the contributions of different processes: $\tau$ , photo electric effect; $\sigma_{\text{coh}}$ , Rayleigh scattering; $\sigma_{\text{incoh}}$ , Compton scattering off an electron; $\kappa_n$ , pair production, nuclear field; $\kappa_e$ , pair production, electron field; $\sigma_{\text{ph}}$ , photonuclear absorption .....	7
<b>Figure 1-5</b> spectrum of positron energy .....	10
<b>Figure 1-6</b> Cross section vs. photon energy for the $\text{O}^{16}(\gamma,n)\text{O}^{15}$ reaction .....	11
<b>Figure 1-7</b> Cross-section vs. photon energy for the $\text{O}^{16}(\gamma,n)\text{O}^{15}$ reaction .....	12
<b>Figure 1-8</b> Resonant energy for giant dipole resonance vs. atomic mass number .....	14
<b>Figure 1-9</b> The probability of eradicating the tumor as a function of dose for Tumors containing $10^6$ , $10^8$ , $10^{10}$ , and $10^{12}$ cells. ....	22
<b>Figure 1-10</b> The probability of curing the tumor and the probability of unacceptable damage to normal tissue vs. dose for a tumor and normal tissue containing $10^8$ cells. ....	22
<b>Figure 2-1</b> Total photon attenuation cross-section in lead as a function of photon energy .....	25
<b>Figure 2-2</b> Block diagram of the set up to observe the output of the linear accelerator .....	26
<b>Figure 2-3</b> Time pick-off unit .....	27

<b>Figure 2-4</b> Output of the linear accelerator vs. time .....	28
<b>Figure 2-5</b> Design of the amplifier used to match the output and input impedances ...	29
<b>Figure 2-6</b> Set-up with the operational amplifier .....	30
<b>Figure 2-7</b> Output of a linear accelerator for a 6MV beam at a dose rate of 600 MU/min .....	31
<b>Figure 2-8</b> Observed output for a 6MV beam at 100 MU/min .....	31
<b>Figure 2-9</b> Components of the radiation time monitor .....	33
<b>Figure 2-10</b> Design of the comparator (LM710B) shown in figure 2-9 .....	34
<b>Figure 2-11</b> Design of the monostable (74123) and the cable driver (74125) shown in figure 2-9 .....	34
<b>Figure 2-12</b> Set up with the radiation time monitor .....	31
<b>Figure 2-13</b> Set up for the proposed experiment .....	32
<b>Figure 2-14</b> Decay of Sodium-22 .....	38
<b>Figure 2-15</b> Decay of Cobalt-60 .....	38
<b>Figure 2-16</b> Decay of Thorium-232. ....	39
<b>Figure 2-17</b> Calibration graph for the multi channel analyzer .....	40
<b>Figure 2-18</b> (a) original - photocathode at a negative high potential .....	41
(b) modified – photocathode at ground potential .....	41
<b>Figure 2-19</b> Set-up for calibrating the detector .....	44
<b>Figure 2-20</b> Set-up for the modified procedure .....	47
<b>Figure 3-1</b> Background activity measured against time .....	51
<b>Figure 3-2</b> Measured activity from the sample of bone after being irradiated by a 6MV beam .....	52
<b>Figure 3-3</b> Decay of 511 KeV photons with time, as measured from the activated sample of CaCO <sub>3</sub> .....	53

<b>Figure 3-4</b> Decay of 511 KeV photons with time as measured from an activated sample of bone .....	54
<b>Figure 3-5</b> Exponential decay of activity from a sample of bone irradiated by 25 MV beam, beam, with the inset showing error bars (random error in the counts) for a few typical points .....	55
<b>Figure 3-6</b> Decay of activity from the sample of bone irradiated with 25 MV beam of photons, with the inset showing error bars (random error in the counts) for a few typical data points .....	56
<b>Figure 3-7</b> Decay of activity from a sample of bone irradiated by an 18 MV beam of photons. The inset shows a few typical points with error bars (random error in the counts) .....	58
<b>Figure 3-8</b> Decay of activity from a sample of tissue irradiated by an 18 MV photon beam. The inset shows error bars (random error) for a few typical points .....	58
<b>Figure 3-9</b> Decay of activity as seen from a bone surrounded by tissue after being irradiated with 18 MV photons. Error bars showing the random in the number of counts are not visible in the scale of the Y-axis .....	59
<b>Figure 3-10</b> Measured activity from a sample of 99.99% calcium after being irradiated by an 18 MV beam .....	61
<b>Figure 5-1</b> Total photon attenuation cross-section in Carbon as a function of photon energy .....	73

# Chapter 1

## Introduction

### **1.1 Available treatment options using photons and their interaction processes**

External beam radiation therapy is a mainstay of treatment option in the treatment of malignant tumors, the other commonly used options being surgery, chemotherapy, and brachytherapy. External beam radiation therapy mainly uses Bremsstrahlung photons produced when highly accelerated electrons are incident on a target of high atomic number, gamma rays produced by radionuclides, and electron beams. The use of heavy particle beams (C-12, protons, etc.) is increasing as they offer radiobiological advantage over photon beams, due to their short ranges and the sharp dose fall-off beyond their maximum range.

In the mega-voltage range of photon beams, the desired biological effect of bond-breaking and hence cell damage of the tumor cells is brought about primarily by the incident photons losing their energy to the tissues of the human body by Compton scattering, pair production and photo disintegration. Photoelectric absorption also contributes but little to the energy loss of the incident photons of the mega-voltage range. Enhancing the local dose delivered by enhancing photonuclear disintegrations offers the possibility of increasing the dose to the tumor (for the same delivered dose) by introducing secondary charged particles in the irradiated region. The dose delivered by

secondary charged particles from the photo nuclear disintegrations that occur in the range of energies available in bremsstrahlung spectrum of photons was attempted to measure to explore the feasibility of local dose enhancement due to photo nuclear disintegrations.

### **1.1.1 Photoelectric absorption:**

The incident photon interacts with an atom and loses all of its energy to the atom. The energy absorbed by the atom is imparted as kinetic energy to an orbital electron, which leaves the atom in an excited and ionized state. The atom returning to ground state is accompanied by emission of characteristic x-rays and / or Auger electrons.

For photon energies that don't lead to highly relativistic photo electrons,  $\tau/\rho$ , the mass attenuation co-efficient (i.e) the beam fraction removed by unit areal density has been calculated to increase as the fifth power of atomic number of the interacting medium and decrease as the seven half power of the energy of the incident photon.<sup>1</sup>

$$\tau/\rho \propto Z^5/E^{3.5}$$

For an interacting medium of low atomic number like tissue with an effective atomic number of 7.4, photo electric effect is negligible with incident photon energies above 200 KeV. In this range of photon energies which are used in radiation therapy, the photo electrons, if they are emitted are relativistic.

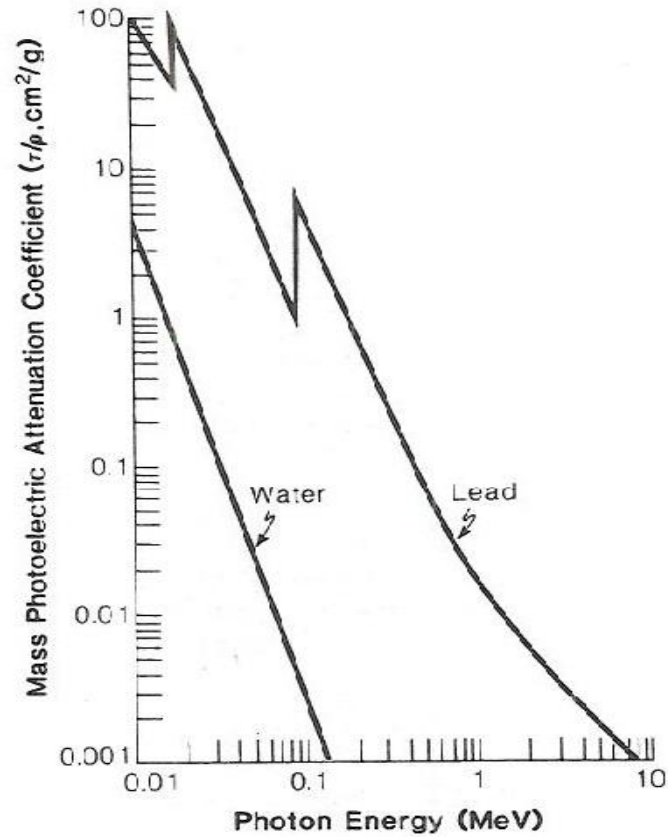


**Fig. 1-1.** Mass attenuation coefficient  $(\tau/\rho)$  vs. photon energy curves for water ( $Z_{\text{eff}} = 7.42$ ) and for lead ( $Z = 82$ ).<sup>2</sup>

The mass photoelectric attenuation coefficient  $(\tau/\rho)$  plotted against photon energy, on a logarithmic scale shows that for water representing a low atomic number similar to tissue, the graph is almost a straight line with a slope of approximately -3.

Experimental data for various materials show that the attenuation coefficient depends on the third power of the atomic number of the interacting medium and decreases as the third power of the energy of the incoming photon.<sup>2</sup>

$$\tau/\rho \propto Z^3/E^3$$

### 1.1.2 Compton scattering:

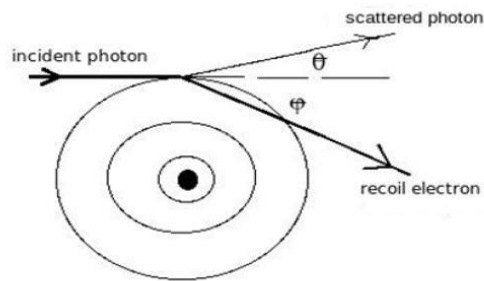


**Fig. 1-2.** Compton scattering

As the photon energy is further increased, the incident photon interacts with a free electron i.e. an orbital electron whose binding energy is negligible compared to the energy of the photon. Part of the incident photon's energy is imparted to the electron

which gets emitted from the atom, and the photon scatters with reduced energy. The lower energy scattered photon is likely to interact with the medium again.

Because this interaction involves free electrons in the absorbing medium, Compton mass attenuation co-efficient ( $\sigma/\rho$ ) is independent of atomic number, Z and is dependent on the electron density of the medium. Number of electrons per gram is about the same ( $3 \times 10^{23}$  electrons per gram) for elements that are of biological interest except hydrogen which has an electron density of  $6 \times 10^{23}$  electrons per gram because of having no neutrons in its nucleus.

### **1.1.3 Pair production**

When a high energy photon ( $E > 1.02 \text{ MeV}$ ) is in the vicinity of a nucleus, some of the incident photon energy can be converted into the rest masses of an electron-positron pair. This would then result in the complete absorption of the photon and the emission of an electron and a positron. According to mass-energy equivalence, the rest mass of an electron or a positron corresponds to energy of 511 KeV. All of the energy of the incident photon, in excess of 1.02 MeV (needed to create the electron-positron pair) is imparted to the pair as kinetic energy with the exception of a very small amount going into the recoiling nucleus.

The electron and the positron, cause excitations and ionization along their range, delivering dose locally. When the positron reaches thermal velocity, it annihilates with an electron, emitting two photons of energy 511 KeV each.



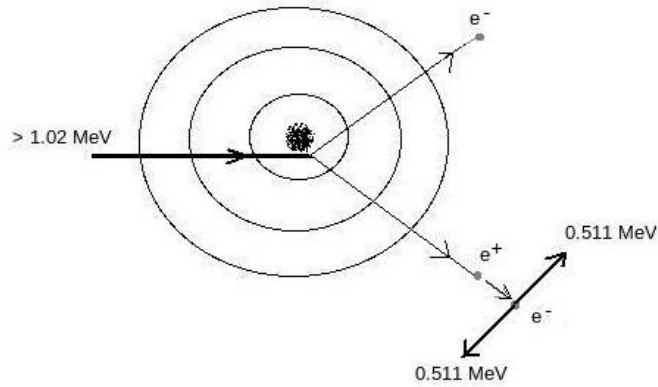


**Fig. 1-3.** Pair production

Because this is an interaction that involves the electric field of the nucleus, the probability of pair production increases rapidly with atomic number,  $Z$  of the interacting material. It varies with  $Z^2$  per atom (and approximately  $Z$  per gram).<sup>3</sup> The probability for pair production increases remarkably as the photon energy is increased beyond the threshold of 1.02 MeV up to about 20 MeV as shown below in figure 1-4.

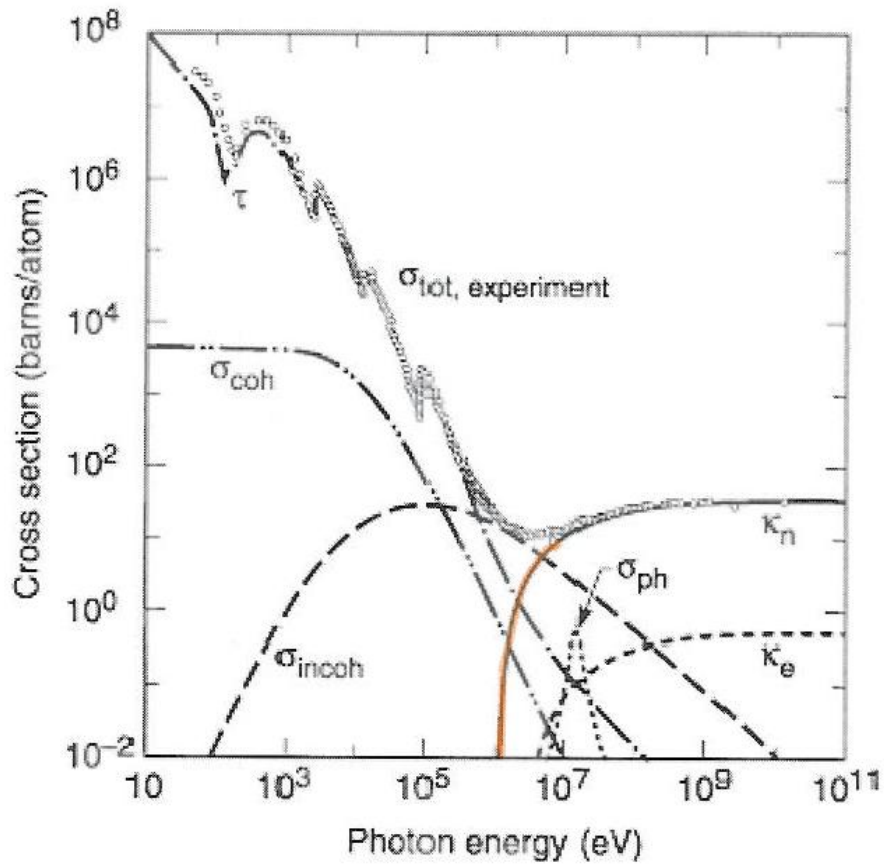


**Fig. 1-4.** Total photon cross section  $\sigma_{tot}$  in tissue, as a function of photon energy, showing the contributions of different processes:  $\tau$ , photo electric effect;  $\sigma_{coh}$ , Rayleigh scattering;  $\sigma_{incoh}$ , Compton scattering off an electron;  $\kappa_n$ , pair production, nuclear field;  $\kappa_e$ , pair production, electron field;  $\sigma_{ph}$ , photonuclear absorption.<sup>4</sup>

#### 1.1.4 Photo disintegration

When the incident photon has enough energy to remove a nucleon from a nucleus, the absorbing nucleus undergoes photodisintegration. The nuclear binding energy being in

the range of 8 MeV or more (except for the lightest elements), this interaction process has a threshold of about 8 MeV. At moderate energies, reactions like  $(\gamma,p)$ , and  $(\gamma,n)$  are initiated. When the incident photon energy is 10 MeV or higher, reactions like  $(\gamma,np)$ ,  $(\gamma,2n)$ , and  $(\gamma,\alpha n)$  are observed.

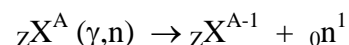
Cross-section for photo disintegration is usually neglected in calculating the energy removed from a photon beam because the cross-sections are small under all circumstances (usually measured in milli barns). They tend to have a sharp threshold, rise to a maximum at 3 to 6 MeV above the threshold and decrease at higher energies.<sup>5</sup>

### **$(\gamma,n)$ reactions**

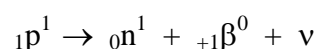
When the incident photon has energy more than the nuclear binding energy, the oscillating electric and magnetic fields of the photon can cause excitation of the nucleus.

The nucleus decays by various methods, one of which is neutron emission.

A neutron being emitted from the nucleus leaves it proton-rich as a result of the  $(\gamma,n)$  reaction.



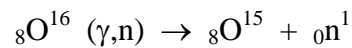
These proton-rich nuclei decay by positron ( $\beta^+$ ) emission, leaving a flux of positrons and neutrons at the site of their production.



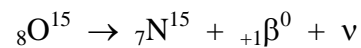
The neutrons, being uncharged are long-range particles and are unlikely to interact locally and hence contribute little to the local dose. The positrons cause ionizations along their range, and hence deliver dose, before attaining thermal velocities and interacting to produce two 511 KeV annihilation photons.

### **$^{16}\text{O} (\gamma, n) ^{15}\text{O}$ reaction**

When this  $(\gamma, n)$  reaction happens with the stable oxygen atoms in tissue and in bone, it leaves behind radioactive  $^{15}\text{O}$ .



$^{15}\text{O}$  decays with a half-life of 2.1 minutes to  $^{15}\text{N}$  by positron emission.<sup>6</sup>



The positrons emitted share the available kinetic energy with the neutrinos, which results in their energy being a spectrum with an end-point energy that corresponds to the difference in the rest mass energy between the initial nucleus and the end products of the reaction, assuming that the recoil kinetic energy of the initial nucleus is negligible. This difference, for the above reaction, gives a maximum energy of 1.73 MeV for the positrons.

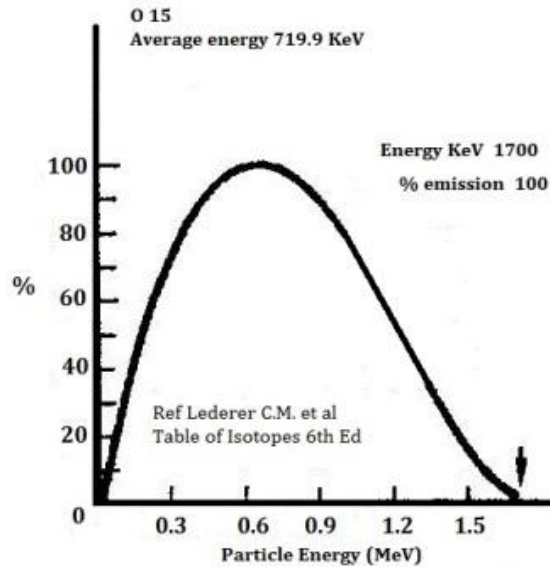


**Fig. 1-5.** spectrum of positron energy<sup>7</sup>

Figure 1-5 shows the spectrum of positron energy of the  $^{16}\text{O}(\gamma, n)^{15}\text{O}$  reaction, with a maximum energy of 1.7 MeV and an average energy of 719.9 KeV.

The reaction cross section versus energy curve shown in figure 1-6 had been obtained by the least-structure analysis of photonuclear yield functions, the number of photonuclear transitions (as evidenced by detection of the resultant nucleons or by counting the resultant activity per unit incident energy at a particular Bremsstrahlung energy) as a function of energy. The data had been acquired in energy intervals of 125 KeV. The numbered peaks had occurred consistently in all cross sections derived from individual yield functions.<sup>8</sup> Cross section of 2 milli barns and lower had been measured up to photon energy of 63 MeV, for this reaction.

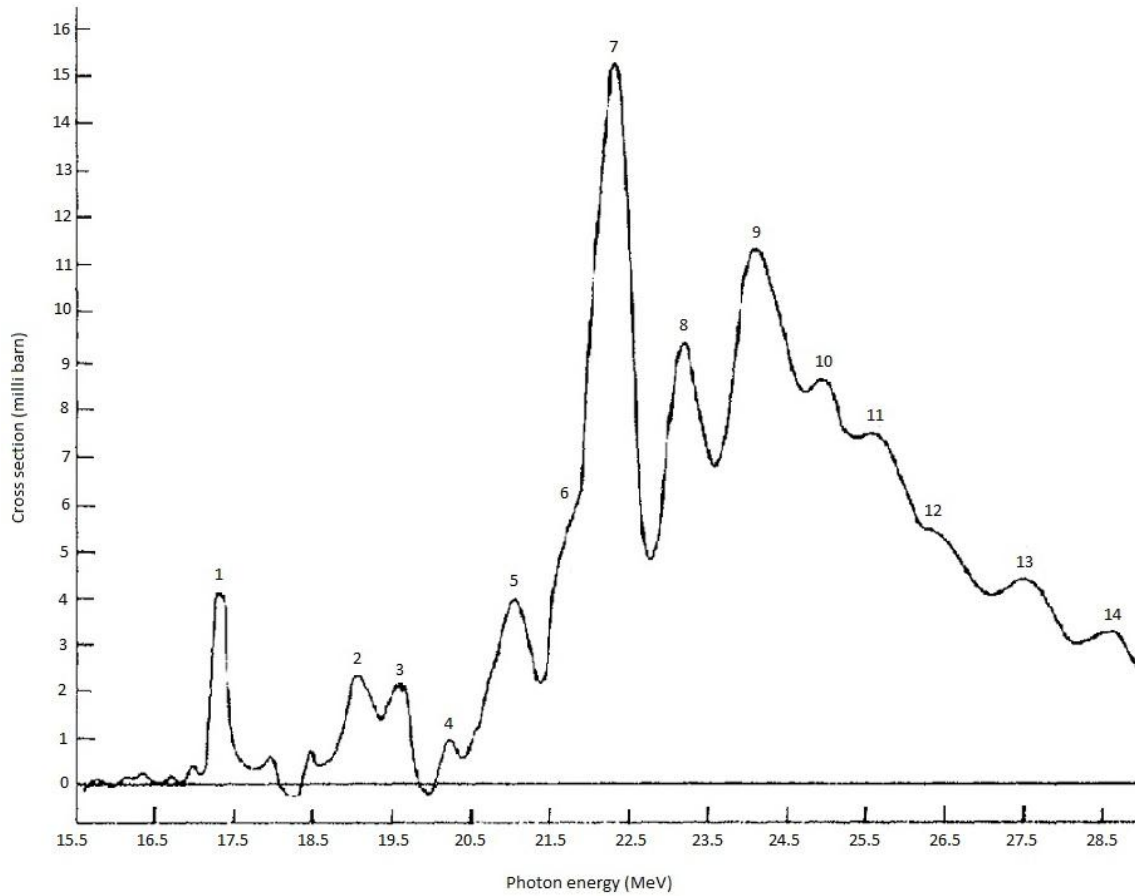


**Fig. 1-6.** Cross section vs. photon energy for the  $O^{16}(\gamma,n)O^{15}$  reaction<sup>8</sup>

The experimental methods for producing beams of monoenergetic photons used for photonuclear reaction studies include annihilation in flight of fast positrons, tagged bremsstrahlung<sup>9,10</sup>, and gamma rays from the capture of protons or neutrons.<sup>11</sup>

The graph of reaction cross section versus photon energy shown in figure 1-7 was obtained by the use of monoenergetic photons from in-flight annihilation of fast positrons.

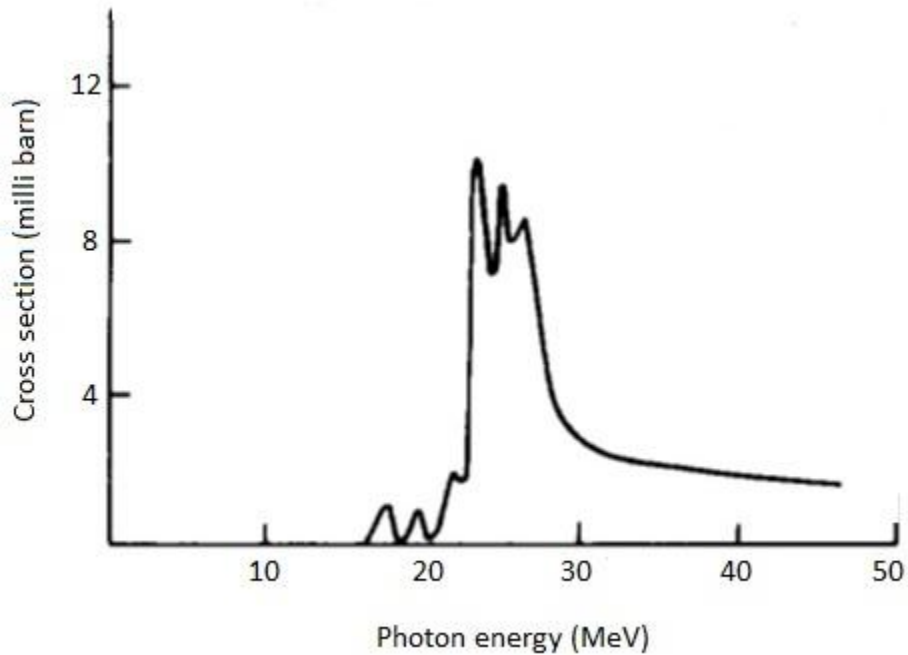
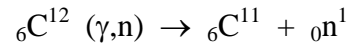


**Fig 1-7.** Cross-section vs. photon energy for the  $O^{16}(\gamma,n)O^{15}$  reaction<sup>12</sup>

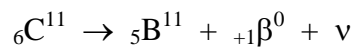
The threshold for this interaction, as seen from figures 1-6 and 1-7 for the  $O^{16}(\gamma,n)O^{15}$  reaction is 15.5 MeV. The reaction has resonances at various higher energies with a maximum cross section of 15 milli barns around 22 MeV. Considering errors in counting statistics, calibration, geometry, and numerical analysis, and assuming random occurrence of these errors, there would be an error of up to 20% in the quoted values.

### **$^{12}\text{C} (\gamma, n) ^{11}\text{C}$ reaction**

When this  $(\gamma, n)$  reaction happens with the stable carbon atoms in tissue and in bone, it leaves behind radioactive  $^{11}\text{C}$ .



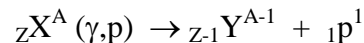
$^{11}\text{C}$  decays with a half-life of 20.1 minutes to  $^{11}\text{B}$  by positron emission.<sup>13</sup>



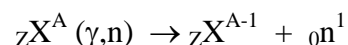
### **Giant dipole resonance**

Giant dipole resonance is an interaction of the electric field of the incident photon and the protons in the nucleus. It is a photo disintegration process where the protons oscillate in response to the alternating electric field of the photon. The neutrons being uncharged are not influenced by the electric field of the incident photon, but being bound to the protons by nuclear force oscillate 180 degrees out of phase with the protons. When this oscillation gains enough amplitude, the nucleus spallates emitting one or more nucleons.

If protons are emitted from the nucleus, the  $(\gamma, p)$ ,  $(\gamma, 2p)$  or  $(\gamma, 3p)$  reactions leave behind proton-deficient nuclei which decay by negatron ( $\beta^-$ ) emission.



Neutrons being emitted from the nucleus will produce proton-rich nuclei which decay by positron ( $\beta^+$ ) emission.





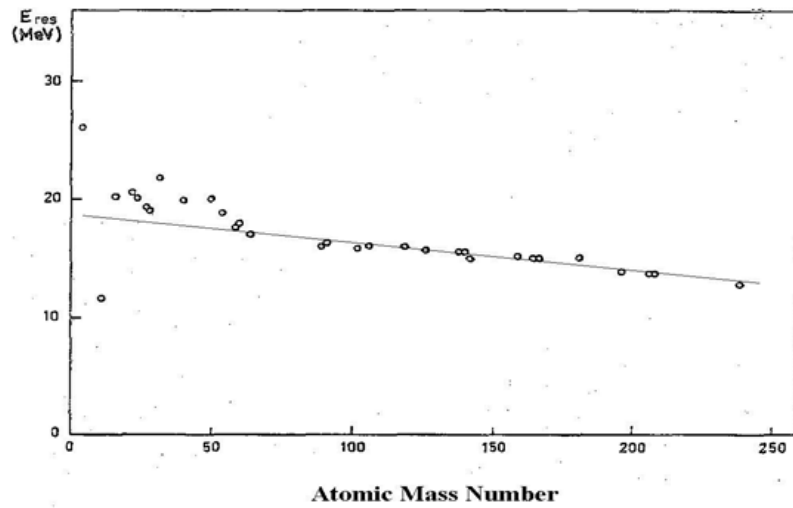
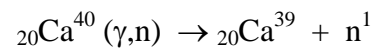
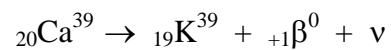


**Fig. 1-8.** Resonant energy (MeV) for giant dipole resonance vs. atomic mass number<sup>14</sup>

For calcium, with a mass number of 40, the resonance is expected around 18-25 MeV as seen from the above figure. Giant dipole resonance of Ca-40 with photons of resonant energy would leave behind radioactive Ca-39 which decays with a half-life of 0.9 seconds<sup>15</sup>.



These radioactive Ca-39 nuclei decay by positron emission to ground state.



The positron emission due to the photo nuclear disintegration processes mentioned above is not a prompt event. In the time between the photon's incidence and the positron's emission, the vibrating nucleus loses information on the direction of the photon's incidence which makes the direction of emission of the positron uncorrelated with the direction of incidence of the photon. The source (i.e) the radioactive nucleus being at rest and the direction of emission of the positron being uncorrelated to the direction of the incidence of the photon, the positrons due to the photo nuclear disintegration processes will be emitted isotropically. Although the main local dose production will be from the positron flux, the endpoint annihilation photons (0.511 MeV) will also deposit dose in the biological material.

All of the common processes by which photons give up their energy involve the production of electrons and/or positrons. Though every molecule can be potentially subjected to radiation damage, only when there is more than one ionization produced within the molecular dimension, is the radiation damage lethal. Single distant ionizations do not contribute to cell damage (because of various cell-repair mechanisms) and hence dose, but contribute to the loss of energy of the incident radiation.

## 1.2 Doping techniques

All of the interaction processes mentioned above depend on the energy of the incident photon with some of them depending on the atomic number of the interacting medium also. Human tissue, with its effective atomic number of 7.64 presents a rather low atomic number medium to the interacting photons, an issue that is addressed by doping techniques like Neutron Capture Therapy and other techniques that selectively enhance absorbed dose in the tumor by concentrating a high atomic number material in the tumor.

### 1.2.1 Neutron Capture Therapy

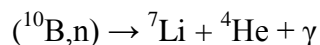
The therapeutic possibilities of neutrons was postulated by Locher in 1936.<sup>16</sup> The technique of neutron capture therapy involves tagging the tumor with a capture agent which compared to other elements present in tissue such as hydrogen, oxygen, nitrogen, etc., has a much higher cross section to interact with neutrons. The tumor is then irradiated with thermal neutrons. The neutrons interacting with the capture agent result in the emission of charged particles which deliver dose locally to the tumor, with minimal dose to the surrounding normal tissue.

Some possible neutron capture agents that have been studied include  $^{10}\text{B}$ ,  $^7\text{Li}$ , and  $^{235}\text{U}$  (radioactive) with cross sections respectively of 3838 barns, 941 barns, and 583 barns for thermal neutron capture.  $^{157}\text{Gd}$  has the highest thermal neutron capture cross section of stable nuclides, at 255,000 barns.  $^{135}\text{Xe}$  with a cross section of 2,720,000 barns for thermal neutrons is an inert gas and is radioactive.

## **Boron Neutron Capture Therapy**

Boron-10, a non-radioactive isotope of boron has been the capture agent of choice for neutron capture therapy, because of its abundance (it comprises approximately 20% of naturally occurring boron), availability, non-toxicity, well understood chemistry, and the fact that B-10 has a cross section of about  $3848 \pm 38$  barns for neutrons of 0.025 eV.<sup>17</sup> It can be preferentially absorbed by the tumor when the tumor is tagged with a drug containing boron-10 and tumor seeking compounds.

A boron-10 nucleus that absorbs a neutron emits a highly energetic alpha particle and a lithium ion.



The alpha particle and the lithium ion are of short range and high linear energy transfer (LET) which is the average energy lost by a particle over a given track length. Their combined path lengths approximates to about 12 microns, one cell diameter – this limits the effects of ionizing radiation to those cells that have been tagged with a sufficient amount of  ${}^{10}\text{B}$ , thus sparing the surrounding normal cells.

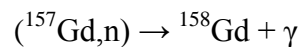
Unlike photons or electrons, alpha particles, with their high LET, can cause bond breaking and hence, cell damage to hypoxic and well-oxygenated tumor cells alike.

They also cause damage to actively dividing and inactive cells alike. Though the tumor is irradiated with an external beam of neutrons, the alpha particles that are released from within the tumor are the primary dose carriers in this technique.

## **Gadolinium neutron Capture Therapy**

Gadolinium-157, with a cross-section of about 255,000 barns for thermal neutrons is being studied as a capture agent<sup>18</sup>, having the advantage of being already used as a clinical agent providing contrast for magnetic resonance imaging.

The (n,  $\gamma$ ) reaction is accompanied by the emission of internal conversion electrons and gamma-induced Auger electrons of varying energy<sup>19</sup>



The low energy Auger electrons provide high LET-type damage within a mean free path of 12.5nm from within the target tissue causing a locally intensive destruction in the DNA of the tumor cells.<sup>20</sup>

The efficacy of neutron capture therapy depends on the selective accumulation of the capture agent in the tumor tissue compared to the surrounding healthy tissue. Various tumor selective Boron / Gadolinium containing clinical agents are being investigated.<sup>21</sup> Studies are also being conducted to detect the prompt gamma rays of the reaction for imaging and hence being able to monitor the uptake region during treatment.<sup>22</sup>

### **1.2.2 Enhancing dose by introducing high atomic number material in the treatment region**

External radiation therapy techniques like intensity modulated radiation therapy offer dose conformity to the target volume. Additional dose conformity and enhancement can be achieved by preferentially increasing the contrast and hence dose inhomogeneity between the tumor and surrounding normal tissue.

### **Dose enhancement by photo electric absorption**

Dose enhancement due to photoelectric absorption of kilovoltage x-rays in elements of atomic number higher than that of tissue had been observed in patients with reconstructive metal implants receiving radiation therapy for mandibular and head and neck cancers, at the metal-tissue interface.<sup>23,24</sup> High atomic number elements have been introduced into the tumor to enhance the local dose by photo electric absorption. Dose enhancing agents that have been investigated include iodine ( $Z=53$ ), gadolinium ( $Z=64$ ), and gold ( $Z=79$ ).<sup>25</sup> Gold, with its high atomic number and biocompatibility<sup>28</sup>, has been studied extensively in the form of nanoparticles and microspheres, to preferentially increase absorbed dose in the tumor.<sup>26-29</sup> With gold nanoparticles, an order of magnitude reduction in the delivered dose has been achieved to deliver the same target dose without the nanoparticles.<sup>29</sup> Comprehensive characterization of cellular responses to the nanoparticles is needed in further assessing their dose enhancing potential in radiation therapy.

The use of flattening filter free (FFF) 6 MV beam has the potential to offer more dose enhancement compared to that of a flattened beam.<sup>30</sup> The FFF beam which has a higher prevalence of lower energy (KeV) photons compared to that of a conventional flattened beam, has a higher percentage of photons at the absorption edge energies of the enhancement elements used, increasing the probability of photoelectric absorption.

### **Dose enhancement by pair production**

With megavoltage photon beams, photon energies of more than 1.02 MeV are available in radiation treatment units. This brings in the possibility of using pair production as the mechanism by which the photon energy is transferred to the interacting human tissue.

The probability of pair production, which depends on the square of the atomic number ( $Z$ ) of the interacting material, increases remarkably as the photon energy is increased up to 20 MeV as highlighted in figure 1- 4. This probability can be further increased by introducing a high atomic number material in the treatment region.

Local dose enhancement of as much as 40% has been achieved by introducing gold ( $Z=79$ ) foils in the treatment region. *In vivo* study of this finding is being done by injecting submicron gold particles into the tumor.<sup>31</sup>

### **1.2.3 Tumor-targeting radiopharmaceuticals**

A radionuclide with its known type of emitted radiation is carried to the tumor by a tumor-seeking carrier.<sup>32</sup> If the range of the emitted radiation is within the tumor, the given dose is restricted to within the tumor, providing a localized radiation dose, from within the tumor, sparing the surrounding normal tissue. The potential use of various liposomes, micelles, microspheres and capsules, etc. as carriers is being investigated.<sup>33</sup>

Nanoparticles of several nature including quantum dots, colloidal gold, super paramagnetic iron oxide crystals, etc. that contain both therapeutic components and multimodality imaging labels are being studied for efficient and specific *in vivo* delivery of the pharmaceutical and for accurate quantitative assessment of the therapeutic efficacy

noninvasively over time.<sup>32</sup> The choice of the radiopharmaceutical would depend on the range and linear energy transfer (LET) of the type of emitted radiation and the half-life of the radioactive isotope. The use of magnetic fields to shorten the range of the positrons and hence to restrict the dose to only the tumor has also been investigated.<sup>34</sup>

### **Metabolic Radiation Therapy**

Radionuclides that intervene in the metabolism of a cell (i.e) in the mechanism of its biological functioning, can be used for therapeutic purposes since their damaging effect will operate within the actual cell itself. <sup>131</sup>I has long been an effective tool for metabolic radiation therapy. Strontium 89, Rhenium 186, and Samarium 153 are some of the radiopharmaceuticals that are being studied for their effectiveness or lack of it in metabolic radiation therapy.<sup>35</sup>

### **1.3 Advantages of local dose enhancement in external beam radiation therapy**

The goal of radiation therapy is to deliver a lethal dose to the tumor while keeping dose to surrounding normal tissue as low as possible. Figure 1-7 shows the graph of the probability for cure against the dose delivered to tumors of various sizes. The steepness of the curves shows that a small increase in dose makes a significant increase in the cure probability.



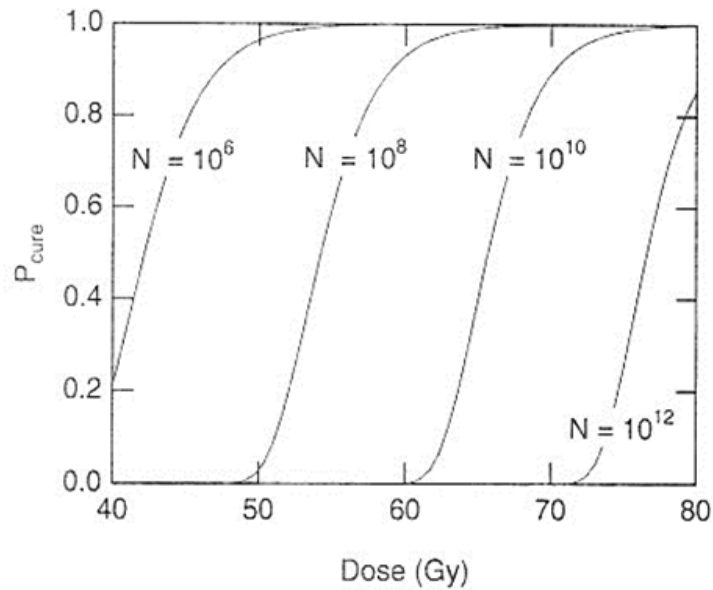


**Fig.1-9.** The probability of eradicating the tumor as a function of dose for tumors containing  $10^6$ ,  $10^8$ ,  $10^{10}$ , and  $10^{12}$  cells.<sup>36</sup>

A limitation of radiation therapy is the potential for toxicity to neighboring normal tissues at an effective dose that offers a high probability for cure, as shown in figure 1-8.

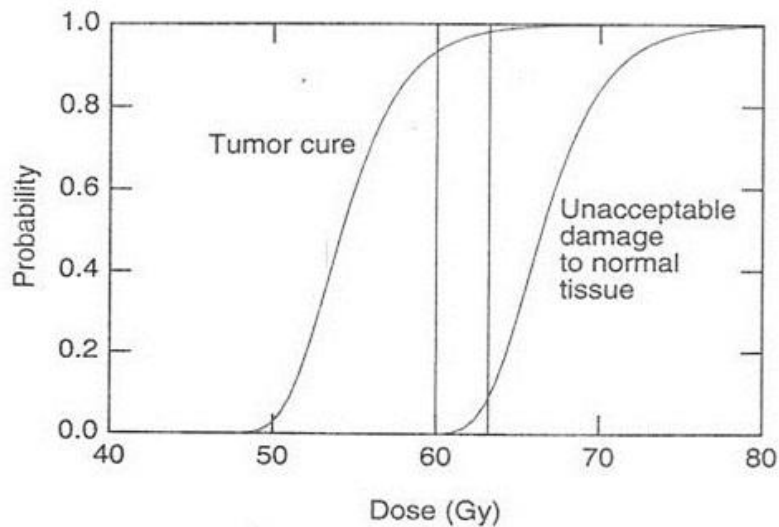


**Fig.1-10.** The probability of curing the tumor and the probability of unacceptable damage to normal tissue vs. dose for a tumor and normal tissue containing  $10^8$  cells.<sup>28</sup>

As seen from the graph, in order to have a high probability for cure, a minimum of 60 Gray delivered to the tumor is required. When the dose is higher than about 63 Gray, there is unacceptable damage to surrounding normal tissue.

When a resonance process that enhances local dose is maximized by using the appropriate energy photons, for a lower delivered dose, the dose to the target can be increased, keeping dose to surrounding normal tissue to a minimum.

## **Chapter 2**

### **Experiment**

#### **2.1 Planned procedure for the experiment**

A known quantity of a calcium compound or bone is to be irradiated using a beam produced at the 25MV setting. Photons are incident on a time pick off unit (fig. 2-2) mounted on to the collimator. When this unit signals the end of incident photon flux, a radiation time monitor (sec. 2.1.3) enables the multi-channel analyzer to start analyzing as soon as the irradiation was complete. The decay products resulting from the interactions of the incident photons with the atoms of the irradiated object will be analyzed using a NaI scintillator coupled with a photomultiplier whose signals are analyzed by the multi-channel analyzer in energy mode in order to detect 511 KeV photons. The 511 KeV photons produced due to the annihilation of the positrons that are products of giant dipole resonance between Ca-40 and photons of resonant energy would be detected after the beam has been turned off (unlike the positrons produced due to pair production, during irradiation).

The same procedure is to be repeated a second time with the analyzer now working in the time mode, with its energy discriminator set for 511 KeV. The decay of 511 KeV photons measured against time is the decay of positrons emitted due to giant dipole resonance after the beam had been turned off. A time analysis of this decay would indicate which radioactive nucleus is decaying by positron emission.

### 2.1.1 Filter to absorb the lower energy photons

The photon beam from the linear accelerator contains a Bremsstrahlung spectrum of energies ranging from zero to a maximum of the accelerating voltage of the electrons. Since the lower energy photons (in the Bremsstrahlung spectrum and Compton scattered photons) do not contribute toward activating the resonance, but toward the externally delivered photon dose (and hence not to the dose enhancement), it is desired to preferentially remove the lower end of the spectrum.

A 3.4 mm thick lead sheet was used to absorb the lower energy photons scattered from the collimator jaws. At very low energy like 0.25 MeV, the lead atoms present a high cross-section of 191 barns/atom<sup>37</sup>, which corresponds to 90% absorption of this energy photons. As can be seen from figure 2-1, photons of energy lower than this have higher cross-sections and are heavily suppressed. As the cross-section increases slowly beyond 5 MeV, a better option is discussed in section 5.2.1.

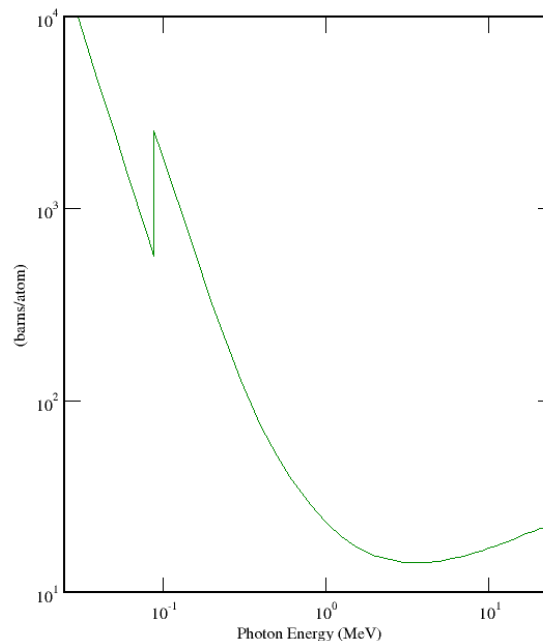


**Fig. 2-1.** Total photon attenuation cross-section in lead as a function of photon energy<sup>37</sup>

### 2.1.2 Output of the linear accelerator

A Varian linear accelerator model 2300cd, with maximum available photon energy of 25 MeV was used for the experiment. The pattern of the output signal of the linear accelerator had to be observed in order to design the radiation time monitor, which will enable the analyzer as soon as the beam had been turned off after having been on.

#### Signals observed

In order to see the pattern of the output of the linear accelerator, a set up as shown in the block diagram below was used.

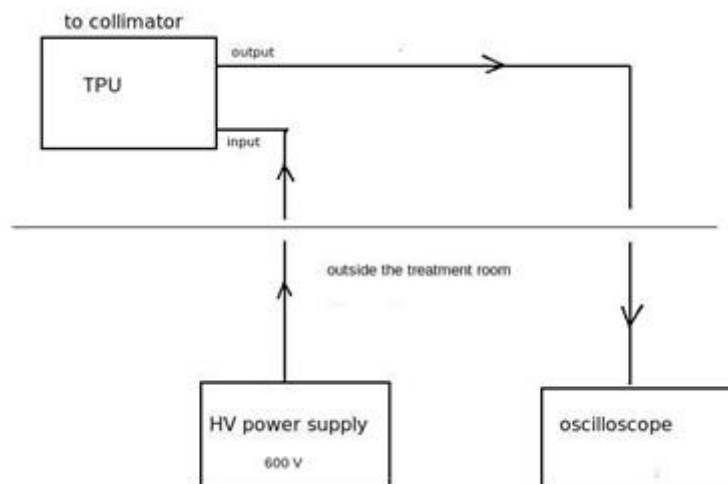


**Fig. 2-2.** Block diagram of the set up to observe the output of the linear accelerator.

The time pick-off unit (TPU) shown in figure 2-2, a device previously constructed, was mounted on to the collimator of the linear accelerator. It consists of a light-tight box with its window made of pure aluminum to avoid any long-lived radioactive isotopes and is painted white inside for maximum reflection. It has a sheet of a plastic scintillator (NE102) at 45 degrees and a side-on photo multiplier tube (1P28) as shown in figure 2-2.

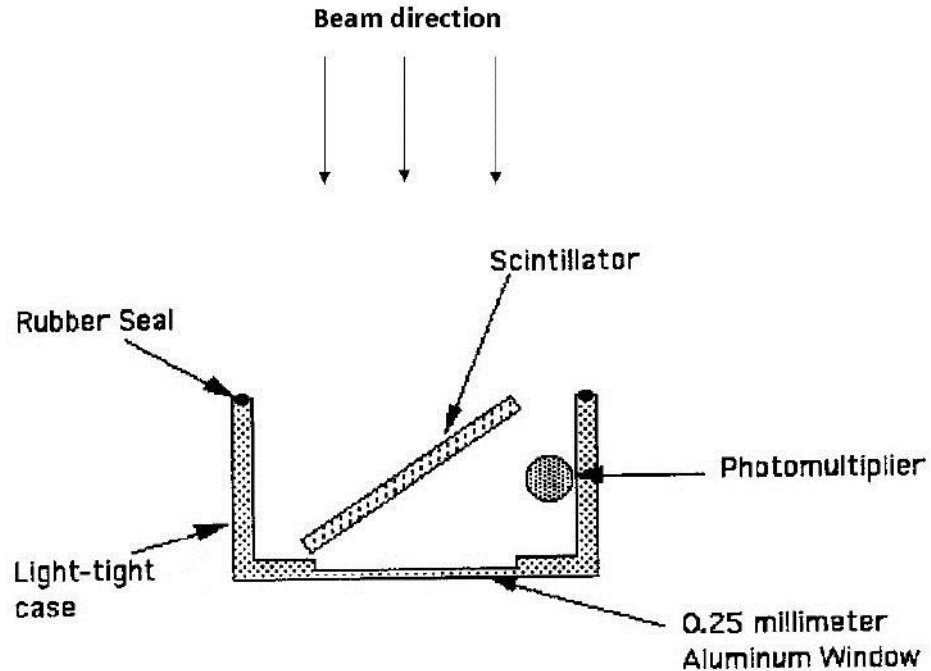


**Fig. 2-3.** Time pick-off unit.

The high voltage power supply that maintains the cathode of the photo multiplier at a high negative voltage with respect to the anode was outside the treatment room and the voltage input to the photomultiplier was done by a long cable passed beneath the door of the treatment room. The output of the photomultiplier was observed on an oscilloscope which was also outside the treatment room and was connected to the time pick-off unit by a long cable passed beneath the door.

As long as there are photons interacting with the scintillator of the time pick-off unit, (i.e) as long as the primary beam is on, the output was observable as a voltage difference on the oscilloscope. The following figure shows the observed output of the linear accelerator for a 25MV beam at a dose rate of 600 MU/min.

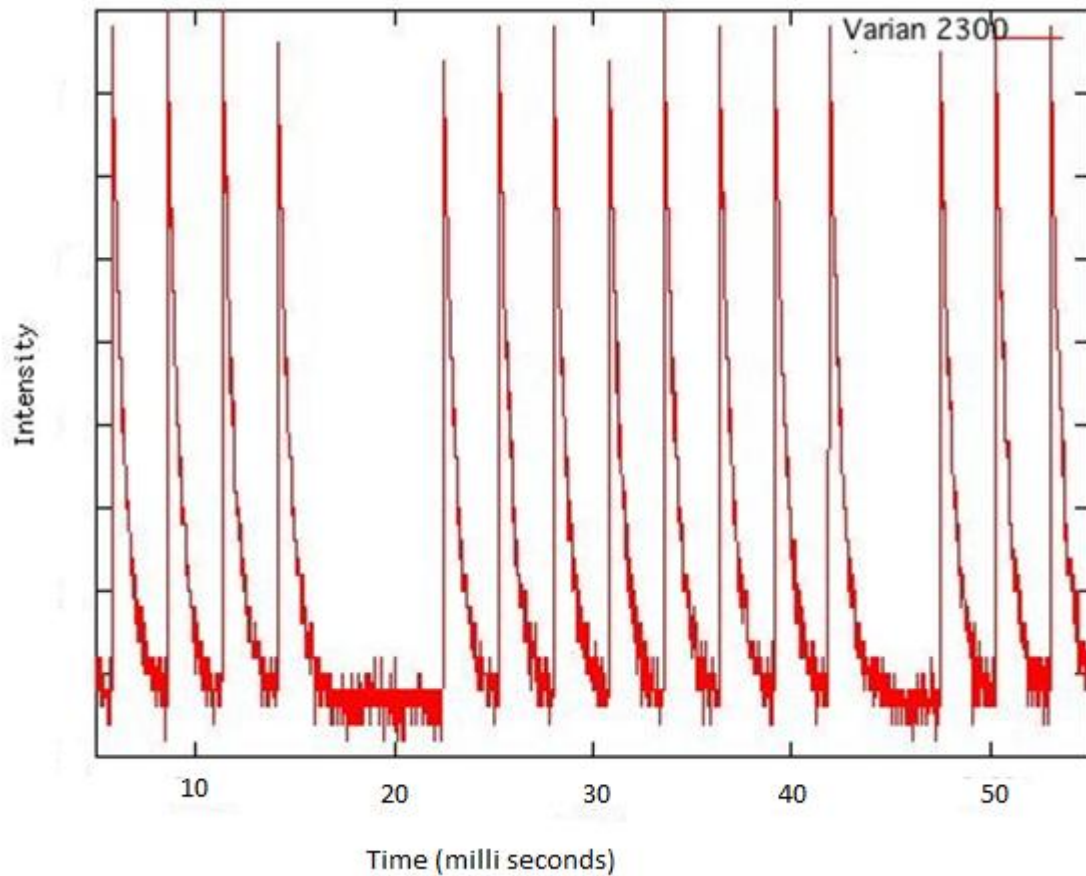


**Fig. 2-4.** Output of the linear accelerator vs. time

As seen in figure 2-4, the output of the linear accelerator was found to be pulsed with occasional longer stretches of noise in between the pulses. Increasing or decreasing the dose rate resulted in the pulses being closer together or farther apart. The signal produced by the activation products was not visible compared to that produced by the primary photons.

It can also be seen that the discharge time for the pulses was about 2 milli seconds which is considerably longer than the rise time due to the stopping transient being longer than the starting transient. It is important to start counting decay activity immediately after

the beam had been turned off because of the short half-lives of the decay products involved. A longer stopping transient would mean a delay in signaling of the beam having been turned off, which in turn, would delay the starting of the counting of decay activity. Having ruled out activation in the aluminum window and the scintillator for possible reasons for the slower discharge, it was attributed to electron charge in the cable discharging through the amplifier of the oscilloscope which is designed to perturb the circuit minimally, and to the possible reflection of the signal in the cable. These were rectified using an external amplifier as a virtual ground.

### Observing the signals using an operational amplifier as a virtual ground

An amplifier with an input impedance of  $50 \Omega$  was constructed in order to match the iterative impedance to the characteristic impedance ( $52 \Omega$ ) of the RG-58 cable used.

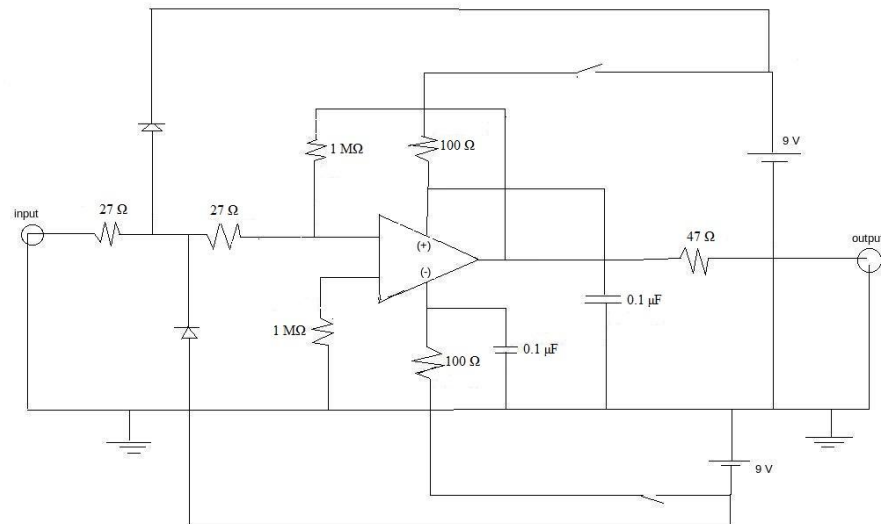


**Fig. 2-5.** Design of the amplifier used to match the input and output impedance



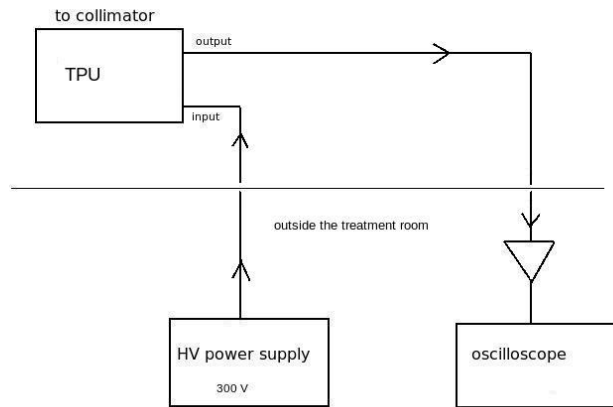


**Fig. 2-6.** Set-up with the operational amplifier

The output from the linear accelerator was observed for a 6MV beam delivered at different dose rates, using the operational amplifier mentioned above as a virtual ground for the co-axial cable.

The following figures show the observed output signals from the linear accelerator with the addition of the cable terminating amplifier.

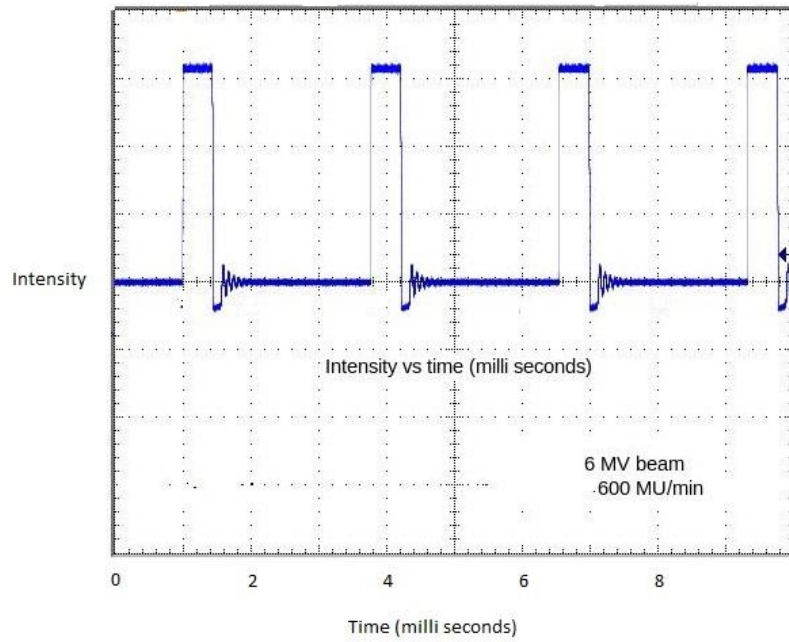


**Fig. 2-7.** Output of the linear accelerator for a 6MV beam at a dose rate of 600 MU/min.

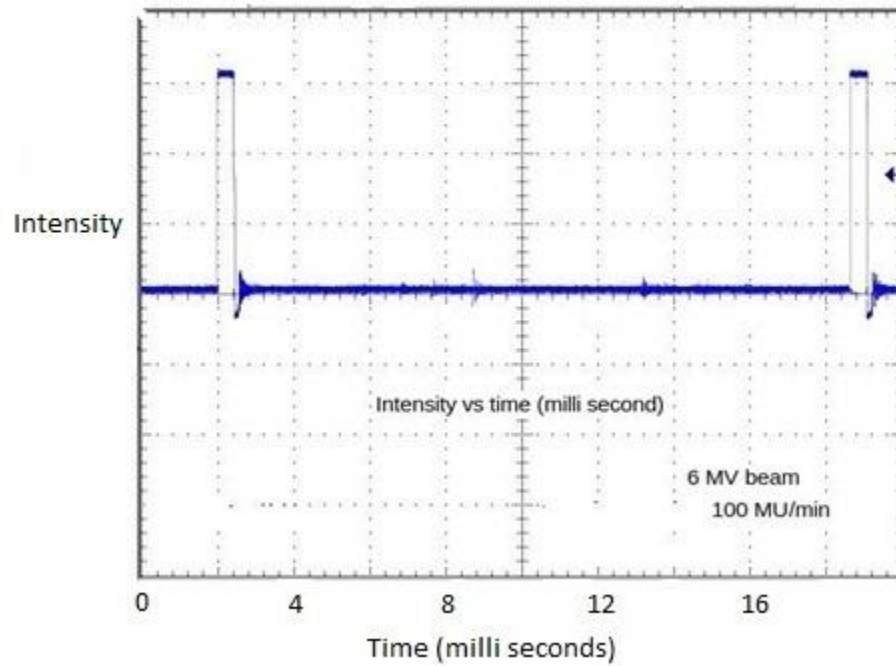


**Fig. 2-8.** Output of the linear accelerator for a 6MV beam at a dose rate of 100 MU/min.

As seen from figures 2-7 and 2-8, the stopping transient which is governed by the time constant of the cable and the resistance of the oscilloscope (1 M $\Omega$ ) is longer than the starting transient by duration of the order of micro seconds. The difference in the duration of the starting and stopping transients is not significant enough to need further rectification. For the purpose of timing to start the decay activity, the signal can be considered to fall off sharply as it does on the rise. The ringing on the fall-off side is a function of the amplifier and does not affect the signalling of the photon beam having been off. The pulses are seen to be broader and closer spaced for higher dose rate and vice versa.

### **2.1.3 Design of the radiation time monitor**

The radiation time monitor is designed to give a signal when the beam turns on and when it turns off. This signal (standard TTL) is fed into the analyzer in order to start the analyzer to measure the decay activity. The components of the radiation time monitor (and their signals) are shown below.

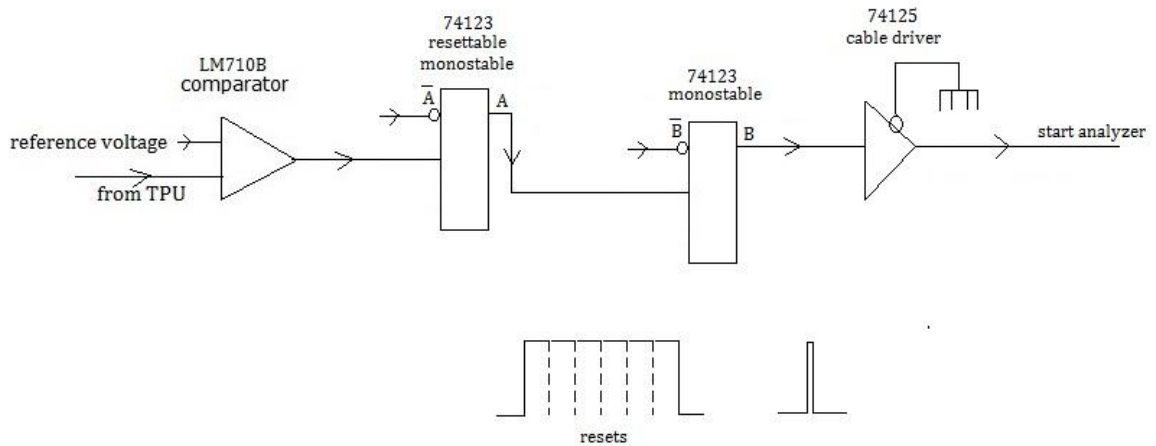


**Fig. 2-9.** Components of the radiation time monitor

As seen in figures 2-7 and 2-8, the pulses from the linear accelerator are of the same height, regardless of the rate of irradiation. It is the width of the pulse that varies according to the dose rate that was set. The threshold for the comparator was set to a third of the voltage (pulse height) of the accelerator output. The comparator first starts but then resets the monostable each time the output of the linear accelerator exceeds the set threshold. When an output pulse is not followed by another pulse (i.e.) the output of the accelerator is below the set threshold for more than 50 milli seconds, the monostable is not reset and gives out a pulse which is used to signal enabling of the analyzer.

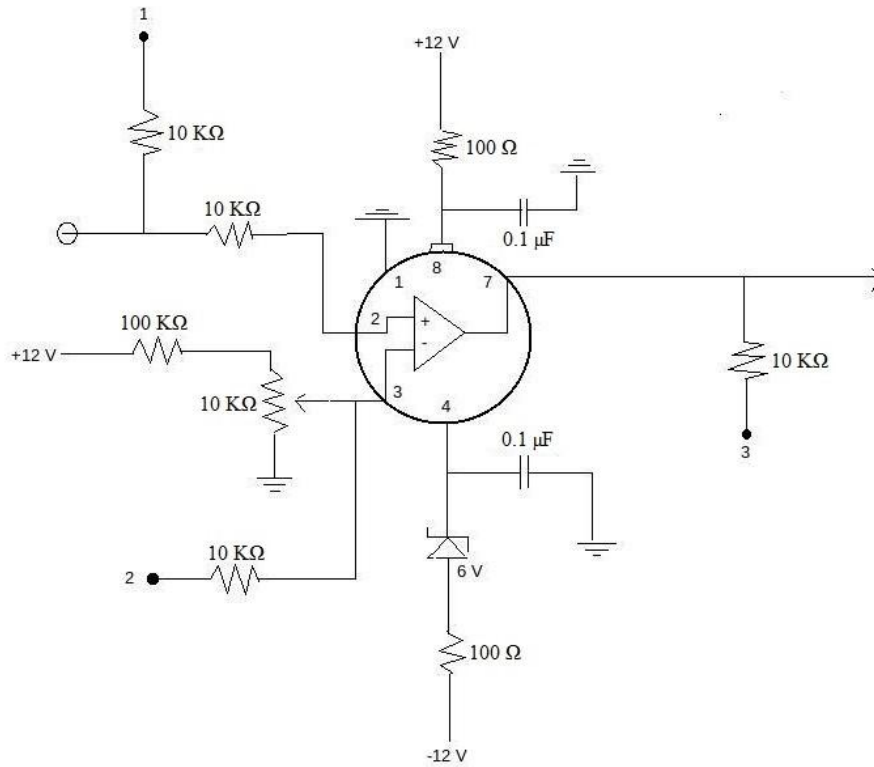


Fig. 2-10. Design of the comparator (LM710B) shown in figure 2-9.

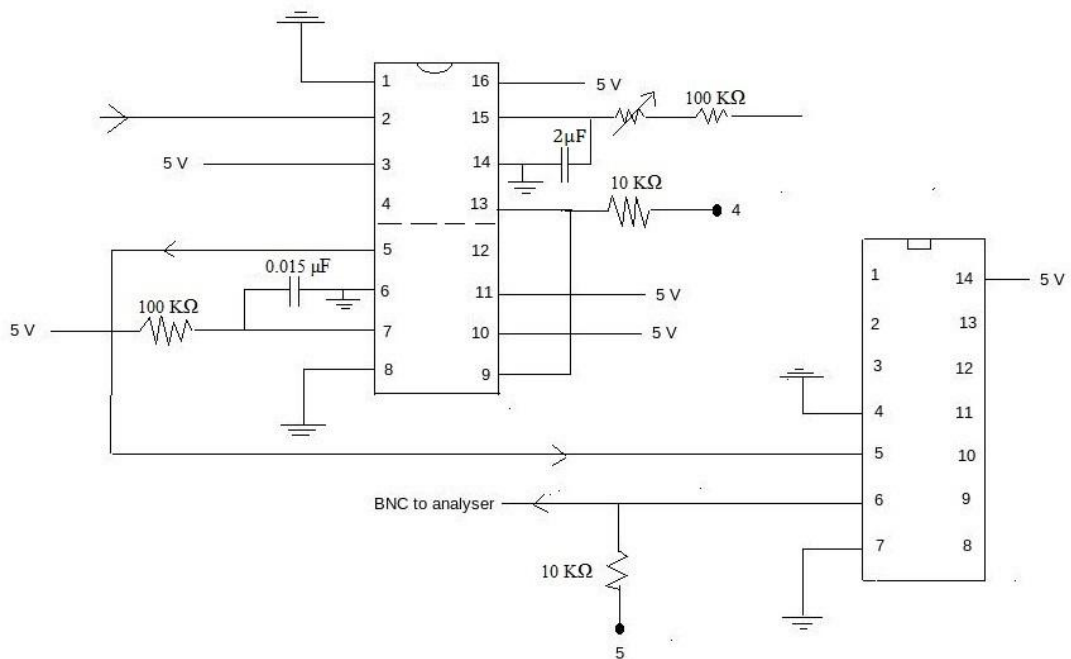
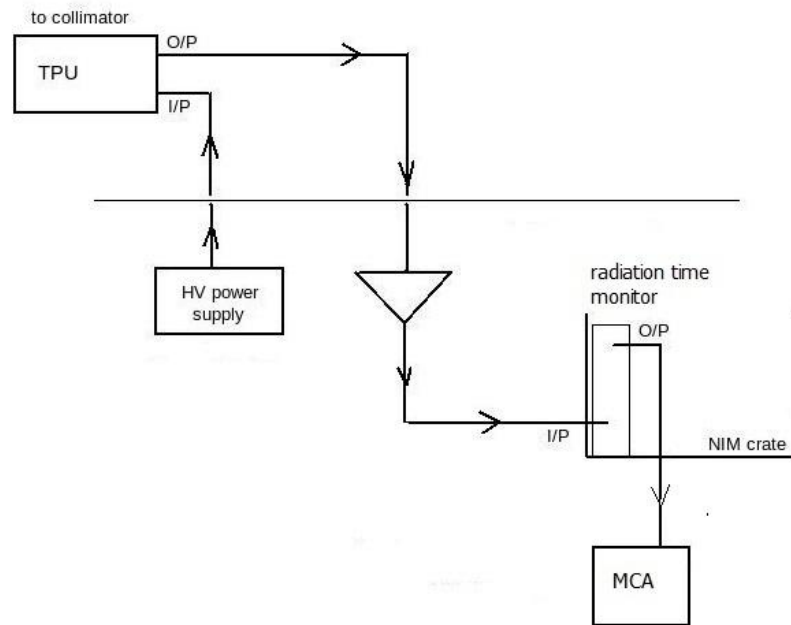


Fig. 2-11. Design of the monostable (74123) and the cable driver (74125) shown in figure 2-9.

Figures 2-10 and 2-11 show the design of the comparator and of the monostable (standard components of an integrated circuit modified to fit the function of the radiation time monitor) which satisfies the condition of the radiation having gone off after having been turned on. Figure 2-12 shows the set up of the radiation time monitor to start the analyzer immediately after the beam had been turned off following irradiation.



**Fig. 2-12.** Set up with the radiation time monitor.

## 2.2 The experiment

Figure 2-13 shows the set up for analyzing the activation products from the irradiated sample. A sodium iodide scintillator coupled with a photomultiplier was used to detect the activation products. The multi channel analyzer would start analyzing the products detected by this scintillator when it receives the signal from the radiation time monitor. Thus, only the 511 KeV photons that result from the annihilation of positrons which are emitted by the proton-rich nuclei as a result of giant dipole resonance between Ca-40 in bone and photons of 15-23 MeV are analyzed by the analyzer.

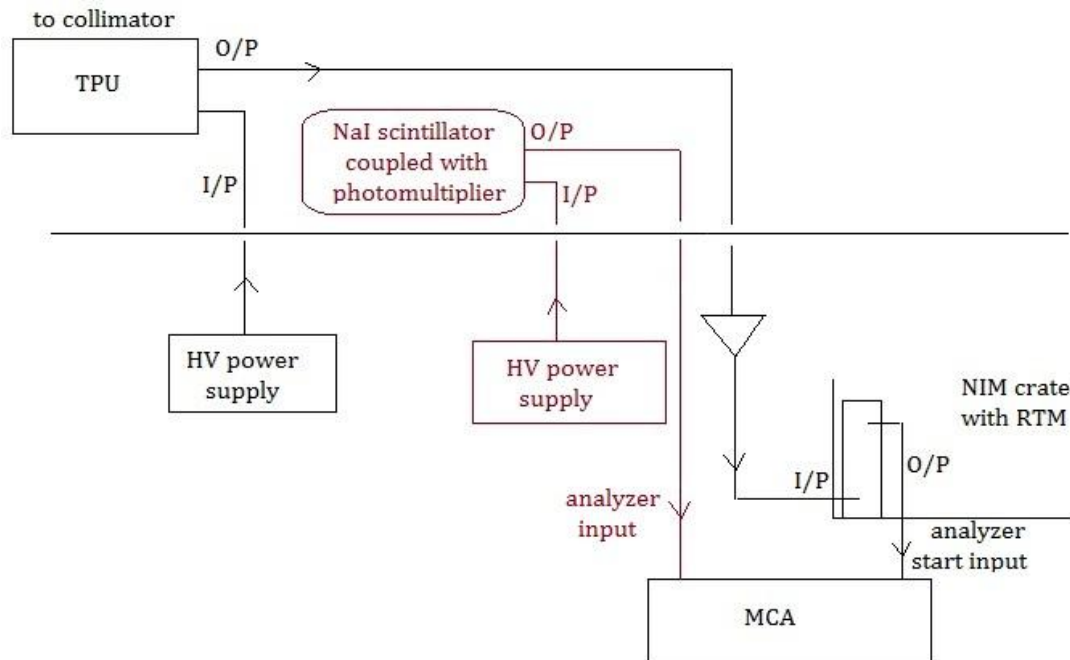


Fig. 2-13. Set up for the proposed experiment

### 2.2.1 Calibrating the multi-channel analyzer

The multi-channel analyzer was calibrated using three sources of known radioactivity, Na-22, Co-60, and Th-232. Peaks corresponding to energy of 511 and 1275 KeV from the Na-22 source, 1170 and 1330 KeV from the Co-60 source, and 300, 543, 873, 1620, and 2117 KeV from the Th-232 source were used to calibrate the multi-channel analyzer. The present activity and half-life, the energies and their emission probabilities of the isotopes used are shown in the table below. The original activity of the Th-232 source was not known and hence, not included in the table. The original activity of the other two calibration sources were known to an accuracy of approximately 2%.

Isotope used	Activity ( $\mu\text{Ci}$ )	Half-life (day)	Energy (KeV)	Emission probability (%)
Na-22	0.00536	950	511	178
			1275	100
Co-60	0.258	1925	1170	100
			1330	100

**Table 2.1** present activity, half-life, energy and emission probability of the isotopes used for calibration.

The following graphs show the semi-log plots of number of counts detected vs. channel number of the analyzer. The radioactive sources were counted for approximately 75 minutes and normalized for 75 minutes in order to obtain good statistics in the peak evaluations.



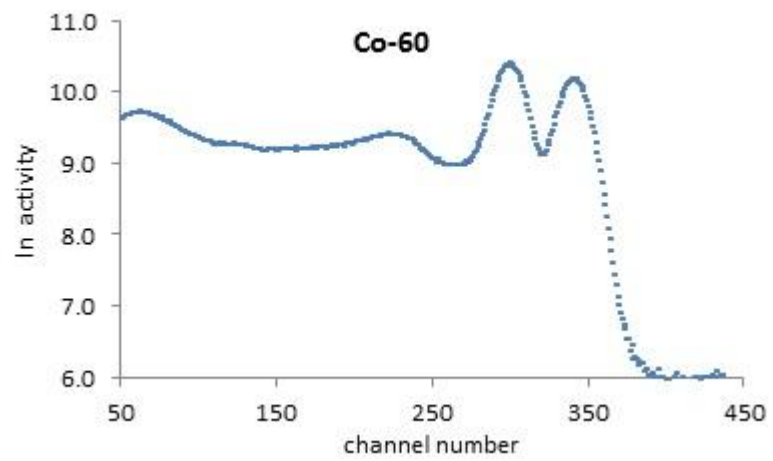
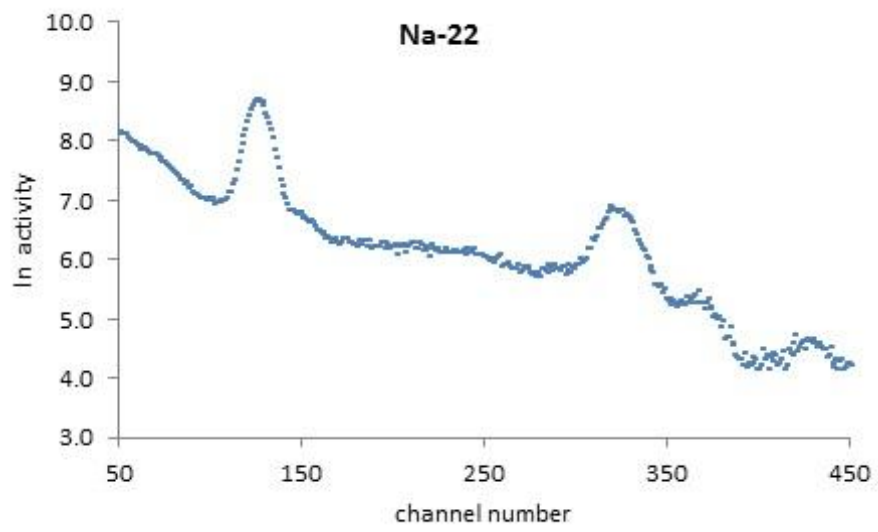


**Fig. 2-15.** Decay of Cobalt – 60.

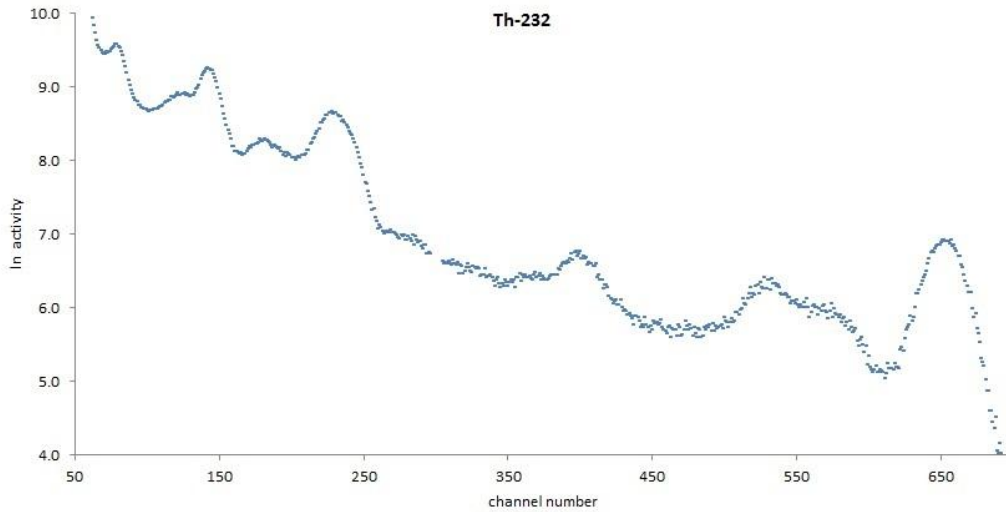


**Fig. 2-16.** Decay of Thorium – 232.

Peak extraction was done assuming the peaks to be Gaussian, the energy deposition by the photons in the scintillator being statistical. The standard deviation in the energy measured from the spectra is shown as the vertical error bars in the calibration graph shown in figure 2-17 below.

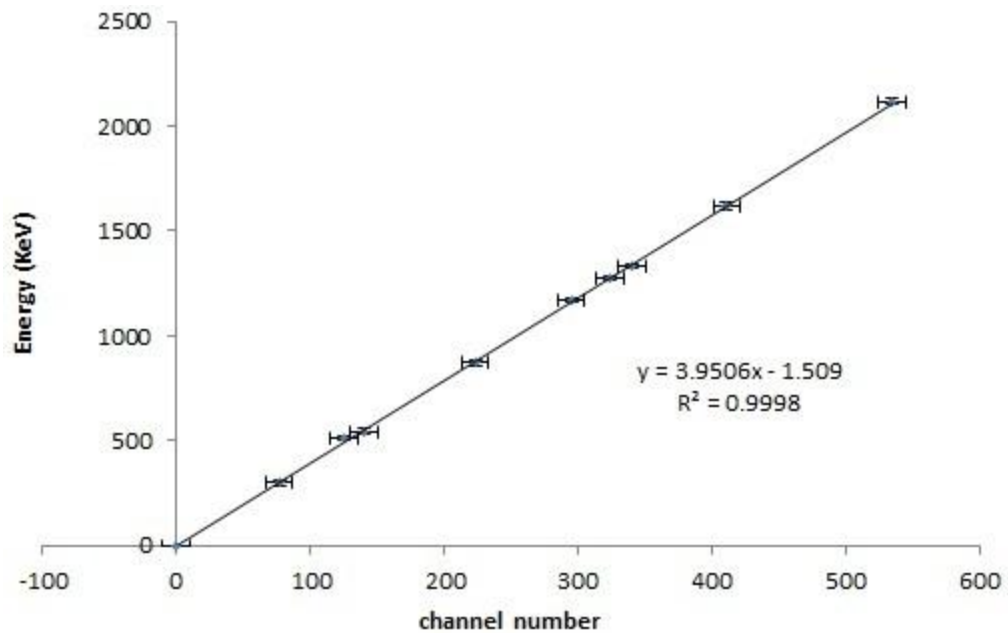


**Fig. 2-17.** Calibration graph for the multi channel analyzer.

The response of the multi channel analyzer was found to be linear in the range of energy shown in figure 2-17. It can also be seen that when 1024 channels are used for the analysis, the peak of 511 KeV is expected to be at channel #129 of the analyzer. The zero level of the analyzer has an instability of less than or equal to  $\pm 0.01\%$  for a 24 hour period at constant temperature and line voltage. Given this electronic wander of the zero level along with the 1% integral linearity of the analyzer, the peak for 511 KeV can be expected to be at channel #129  $\pm 10$  channels.

When the analyzer is used in quarters (256 channels each) for the energy decay analysis, the peaks of 511 KeV can be expected at channels 32, 288, 544 and  $800 \pm 3$  channels.

### 2.2.2 The detector

The thallium doped sodium iodide [NaI(Tl)] scintillator used is 3 inches (76 mm) in diameter and 4 inches (102 mm) long. It was coupled with a photomultiplier whose power system was modified so that the photocathode was at ground potential rather than being at a negative potential (-1300 volts) in order to make the electric field uniform at the photocathode.

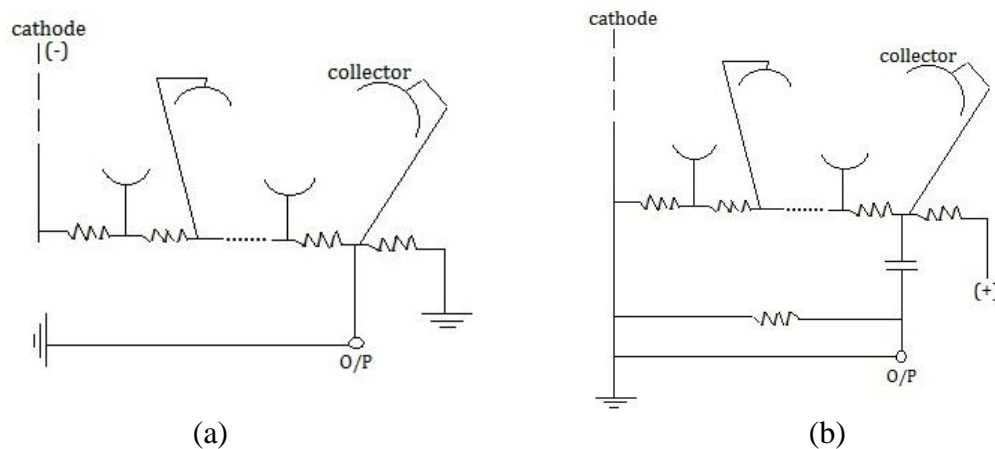


**Fig. 2-18.** (a) original - photocathode at a negative high potential. (b) modified – photocathode at ground potential.

As shown in figure 2-18, the original negative potential for the photocathode was modified to be at zero and in order to be able to see the output of the photomultiplier onto an oscilloscope, a coupling capacitor was added to the detector chain.

### **Measured detector parameters**

The detector had an *intrinsic efficiency* (gross detection efficiency) of 20% which is typical for a crystal of the size used. This was determined using the background subtracted Co-60 spectrum.

The following table shows the *peak to Compton ratio* for an uncollimated isotropic radiation source obtained with the detector with the photon energies employed for calibrating the multi channel analyzer when set to pulse height analysis.

<b>Energy</b>	<b>Peak to Compton ratio</b>
2.5 MeV	1.1
1.2 MeV	1.8
0.7 MeV	2.5

**Table 2.2** Peak to Compton ratio obtained with the NaI detector.

Detecting photons of energy 511 KeV from the activated sample and measuring the rate of decay of the 511 KeV photons is a significant part of the experiment. The detector having a high peak to Compton ratio at an energy closer to 511 KeV (700 KeV, in the table) is helpful for the experiment.

The activation products from the experimental sample will not be collimated in order to avoid detecting activation products from the collimator and also in order to detect as many photons from the activated sample as possible.

For an uncollimated source that emits isotropically, the detector had a *relative resolution* of 10.1% at 511 KeV, the photon energy of interest. Relative resolution was determined using the full width at half maximum of the photo peaks in the spectra used for calibration. The following table summarizes the relative resolution and the resolution efficiency of the detector found using the two calibration sources at the expected working distance.

<b>Energy</b>	<b>Relative Resolution</b>	<b>Detection efficiency</b>
511 KeV	10.1 %	16.6 %
1170 KeV	6.2 %	4.9 %
1275 KeV	6.1 %	5.3 %
1330 KeV	5.4 %	3.6 %

**Table 2.3** Relative resolution and resolution efficiency of the detector

As can be seen from table 2.3, the detector has a higher *detection efficiency* (full-energy or photo peak efficiency) at 511 KeV compared to that at higher energies. The photo electric interaction is the predominant interaction process at lower photon energies, with more of the incoming photon energy being deposited in the full energy peak compared to the higher energy photons that are Compton scattered.

### 2.2.3 Calibrating the detector

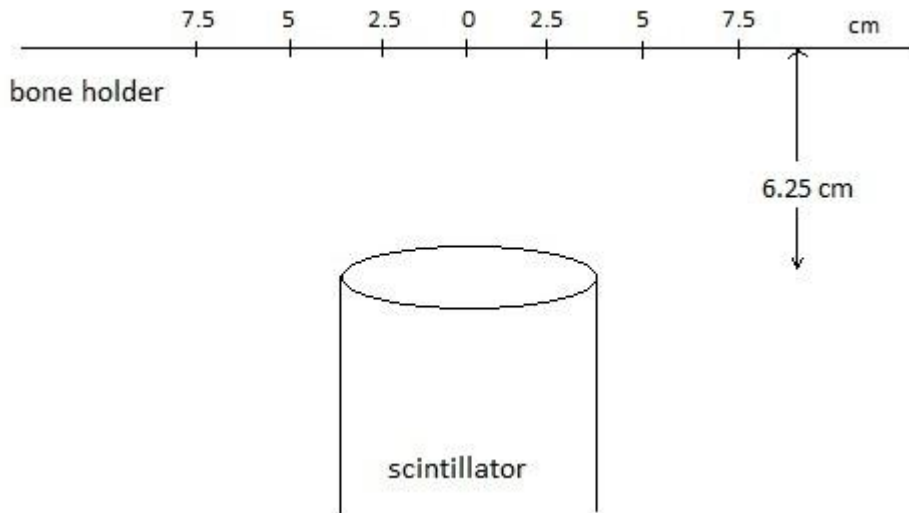


**Fig. 2-19** Set up for calibrating the detector

A device was made to hold the irradiated sample in front of the detector at 6.25 cm. It was made of polystyrene, avoiding metal screws. It had openings on the sides that the bone could be quickly and easily inserted through, so it held the bone in front of the detector without anything in between the bone and the detector. The detector was calibrated with a radioactive Na-22 source of known activity placed at different points on the holder in order to know what fraction of the radiation emitted from the activated sample is detected.

At the center (marked 0 cm), the detector of radius 3.8 cm has its edges at a distance of 7.3 cm from the center of the bone holder, subtends a solid angle of 0.9 steradians and is expected to count roughly 7% of the radiation (511 KeV photons) emitted by the isotropic source, and was found to detect 10.5% of the emitted 511 KeV

photons. At 5 cm on either sides of the center, the detector was able to count 10-12% of the radiation emitted by the source. At 7.5 cm on either sides, the detector counted 8% of the emitted 511 KeV photons.

#### **2.2.4 Sample to be irradiated**

An experiment sample was made of calcium carbonate ( $\text{CaCO}_3$ ) contained in a thin plastic vial that was available. Plastic was chosen because of its low atomic number. As the components of the plastic vial was not known, the empty vial was irradiated and made sure that it showed no activation. Calcium carbonate was chosen since it contains more calcium per unit volume compared to that of a real bone. More calcium in the sample is desired in order to see a higher yield of positrons from the giant dipole resonance of Ca-40 with the photons of the appropriate energy. The sample consisted of 25.5 grams of calcium carbonate, placed in a cylindrical container measuring 15 cm in length and having a radius of 1 cm. After testing the experimental procedure using this sample, the experiment was done in a real bone also in order to estimate dose enhancement in bone due to giant dipole resonance of calcium in bone with the resonance energy photons in the beam.

#### **2.2.5 The various trials**

As shown in figure 2-13, the detector is in the treatment room in order to detect the activation products from the irradiated sample. The recovery time of the detector is in the order of micro seconds (0.23 micro seconds for the NaI crystal, along with a recovery time of a few micro seconds for the associated electronics). Because of this short



recovery time, the scintillator being saturated with events during the time that the beam is turned on was not thought to be of concern. The activation products in the room following an irradiation at the 25 MV setting have a maximum energy of about 2 MeV<sup>30</sup>. In order to make this background smaller, for the scintillator to not be saturated immediately following the irradiation, the detector was shielded in an enclosure made of lead bricks which provided shielding thickness of up to 20 cm.

Various positions and configurations of the detector and the enclosure were tried in order to be able to detect the signal from the activation products of the sample above the signal from background in the room following the irradiation. The collimator jaws and the flattening filter in the linear accelerator head and the treatment couch being also sources of neutrons<sup>31</sup> as a result of photo nuclear reactions that follow a high energy irradiation, various gantry positions were tried along with the different configurations of the detector and its shielding enclosure. Trials were also done with the detector set up in the maze where the irradiated sample can be pneumatically transported to. The scintillator was found to be saturated by the induced back ground activity in the room in all of the above-mentioned trials due to products of the photonuclear and neutron capture reactions that are consequences of a high energy irradiation. Neutron shielding was not used as the saturation was due to induced back ground activity and also because NaI as a crystal detector, does not have a high sensitivity to neutrons.

Having done differential trials to rule out the possibility of the leakage current in the capacitor due to radiation damage and activation in the components of the detector or in the lead blocks used for shielding the detector, the scintillator being saturated was attributed to high induced activity in the room (from the gantry components and from the

construction materials of the walls) immediately after a 25 MV beam had been turned off. This induced activity produced a signal that was too high to be able to detect the signal from the activation products of the sample. This was further confirmed by the fact that the scintillator was found to be not saturated following an irradiation done at a peak voltage of 6 MV. Since the photon energy of the resonance needs energies between 15 and 25 MeV, the irradiation needs to be done with the linear accelerator operating at a peak voltage of 25 MV in order to induce the resonance. The original procedure was therefore modified so that the experiment can be done using a radiation beam obtained at a peak voltage of 25 MV and to be able to detect signals from the activated sample above the signal due to activation in the room, the highest source of activation being the components (collimators, filters, etc.) of the accelerator itself and the construction materials of the walls of the room.

### 2.3 The Modified procedure

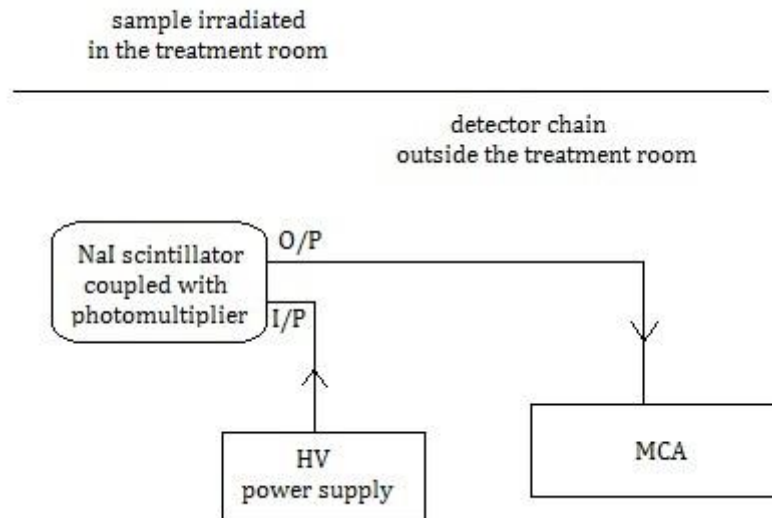


**Fig. 2-20** Set-up for the modified procedure

As shown in figure 2-21, the detector and the associated electronics were kept outside the treatment room, in order to avoid the high induced background activity in the room due to the high flux of neutrons following an irradiation at the 25 MV setting. The sample, following the irradiation would ideally be pneumatically transported to the detector in order for the activation products to be counted. However, because of the unavailability of pneumatic transport, the irradiated sample will be manually carried over to the detector, following safe practices of distance and time, with the transit time being recorded. The detector being outside the treatment room and the sample being brought out to the detector after the termination of the irradiation makes the use of time pick-off unit and the radiation time monitor unnecessary. Bringing the irradiated sample out to count also meant that the only activated radioactivity in the vicinity of the detector is the activation from the sample.

Therefore, this procedure was carried out with the detector outside the treatment room. When the irradiated sample of calcium carbonate was brought out to the detector to be analyzed, a 511 KeV peak was observed against the general background. The decay of this peak was observed at different times in the different quarters of the analyzer memory, the analysis of which is shown in the next chapter. When this procedure was repeated with the analyzer working in the time mode, the decay of activity was observed against time. An analysis of the decay of counts of the activation products against time will help identify the nuclear series that is decaying by positron emission following a photo disintegration process.

### **2.3.1 Trial 1**

The detector chain was set up as shown in figure 2-21. The multi channel analyzer, in its energy mode, was set to count for 20 seconds each in four quarters. The linear accelerator (Varian 2300 cd) was set to deliver a beam at a peak voltage of 25 MV, at a dose rate of 600 monitor units per minute. The vial of calcium carbonate was set at 100 cm source to surface distance and irradiated with a field size of 3 x 15 cm for 20 seconds. The irradiated and activated sample was manually brought out from the treatment room, following procedures as stated, and placed in the holder in front of the detector. The decay of the induced activity in calcium carbonate was observed with the analyzer working in its energy mode in order to detect the 511 KeV photons. The same procedure was then repeated with an avian (flightless) bone irradiated at the same setting. Avian bone was chosen because of the availability of fresh and uncut bone. As birds of flight tend to have more hollow bones than that of flightless birds, flightless avian bone was chosen.

Using the same set-up parameters and irradiation conditions, the bone was irradiated the next day and the decay of the induced activity was recorded with the analyzer working in its time mode. In addition, to measure the increase in dose due to the decay of activation products, thermoluminescent dosimeters (TLD) of lithium fluoride of 1 mm x 1 mm x 1mm were used to measure dose in tissue surrounding bone and in boneless tissue. The TLDs were known to have a sensitivity 10 pGy to 10 Gy.

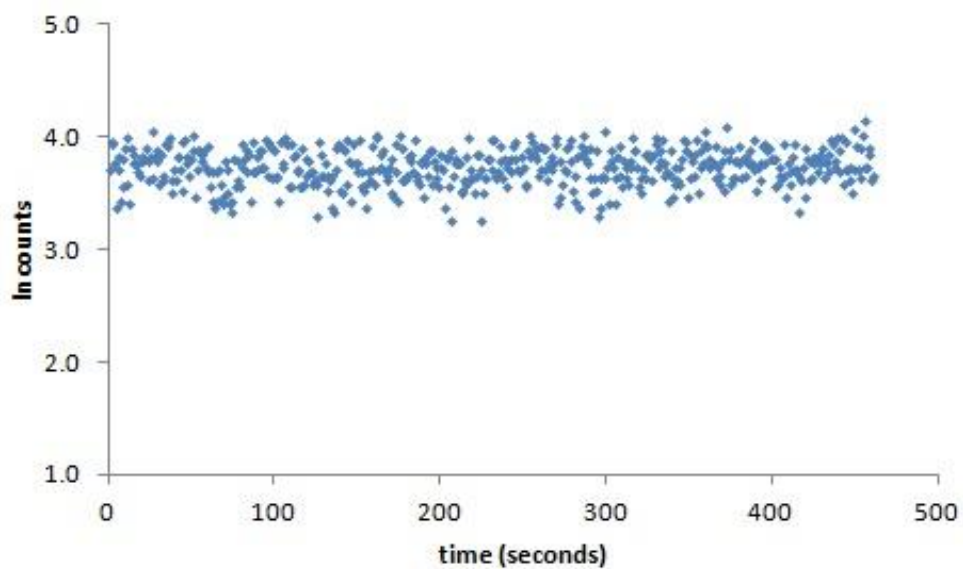
### **2.3.2 Trial 2**

A second trial was performed using a beam at a peak voltage of 18 MV and a dose rate of 600 monitor units per minute. 200 monitor units were delivered to the vial of 99.99% pure calcium set at 100 cm source to surface distance. The decay of the irradiated and activated sample was measured with the analyzer working in the time mode. Using the same beam parameters, 0.034 Kg of bone, 0.346 Kg of tissue, and 0.456 Kg of bone surrounded by tissue were irradiated.

# Chapter 3

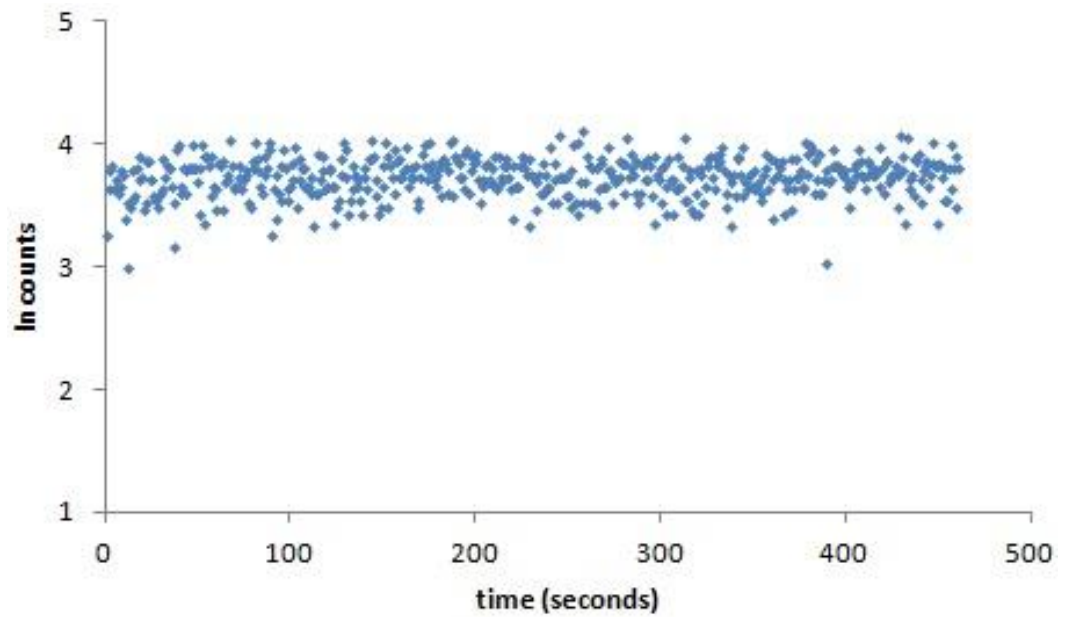
## Analysis and Results

### 3.1 Analysis of data



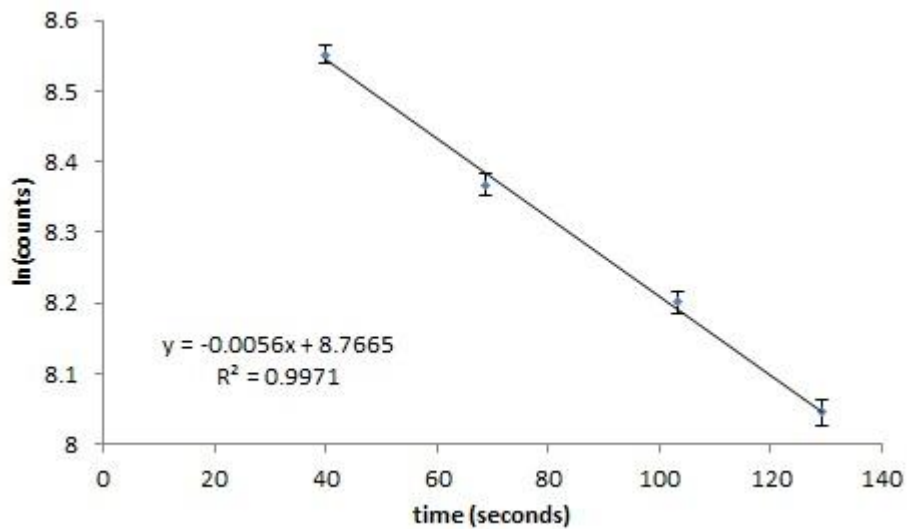
**Fig. 3-1.** Background activity measured against time.

Figure 3-1 shows the background activity that was measured before the start of the experiment. The background was found to be steady.



**Fig. 3-2.** Measured activity from the sample of bone after being irradiated by a 6MV beam.

Figure 3-2 shows the activity that was measured from the sample of bone that was irradiated with a 6MV beam. The sample showed no activation, as expected, as it requires a photon energy of 8 MeV or more for activation in the sample, given that neutron binding energy in most nuclei is approximately 8 MeV.



**Fig. 3-3.** Decay of 511 KeV photons with time, as measured from the activated sample of CaCO<sub>3</sub>.

Figure 3-3 shows the decay of 511 KeV photons from the activated sample of calcium carbonate, with error bars showing random error (square root of counts) in the measured counts. The vial containing the sample was irradiated using a 25MV beam. The residual activity was counted for nearly two and half minutes with the multi-channel analyzer set to detect and count 511 KeV photons. The decay of 511 KeV photons with time, on a semi-log plot, gives a half-life of  $124 \pm 0.1$  seconds. The uncertainty in the measured value of half-life arises from variations in human reaction times, as estimated by repeated simulated measurements of different time intervals of the decay being counted in the different quarters of the multi channel analyzer.



The measured half-life of  $2.07 \pm 0.002$  minutes corresponds to the decay of  $^{15}\text{O}$  from the  $^{16}\text{O}(\gamma, n)^{15}\text{O}$  reaction with a half-life of 2.05 minutes.<sup>6</sup>

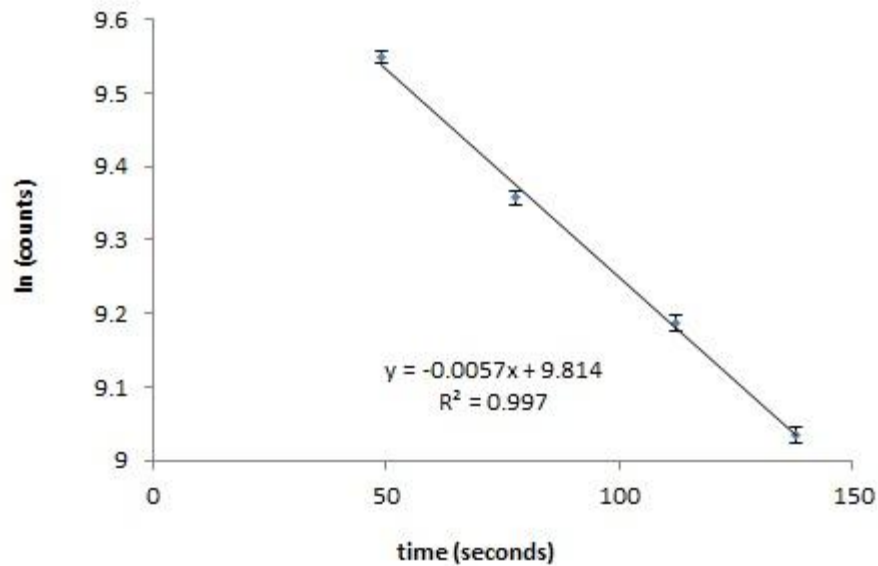


**Fig. 3-4.** Decay of 511 KeV photons with time as measured from an activated sample of bone.

The above figure shows the decay of 511 KeV photons from a sample of bone activated using a 25 MV beam of photons. As with the sample of calcium carbonate, the residual activity was counted for about 150 seconds with the multi-channel analyzer set to detect and count 511 KeV photons, the error bars showing random error (square root of counts) in the measured counts.

The decay of 511 KeV photons with time, on a semi-log plot, gives a half-life of  $122 \pm 0.1$  seconds, the uncertainty in the measurement of which is as discussed in the previous page. This measured half-life of  $2.03 \pm 0.002$  minutes, again, shows the decay of  $^{15}\text{O}$  which has a half-life of 2.05 minutes, from the  $^{16}\text{O}(\gamma, n)^{15}\text{O}$  reaction.

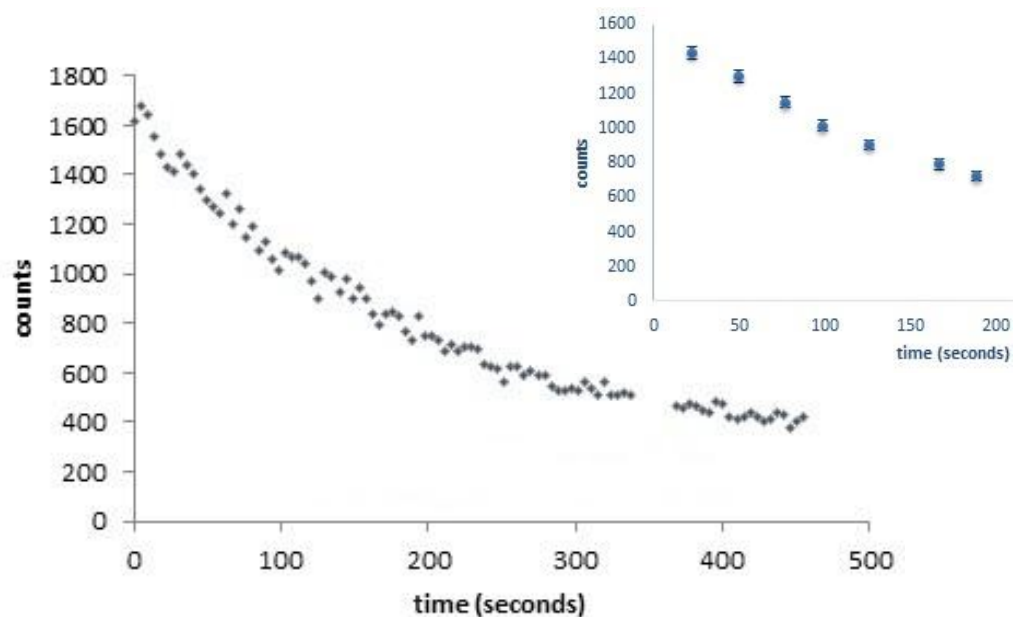


**Fig. 3-5.** Exponential decay of activity from a sample of bone irradiated by 25 MV beam, with the inset showing error bars (random error in the counts) for a few typical points.

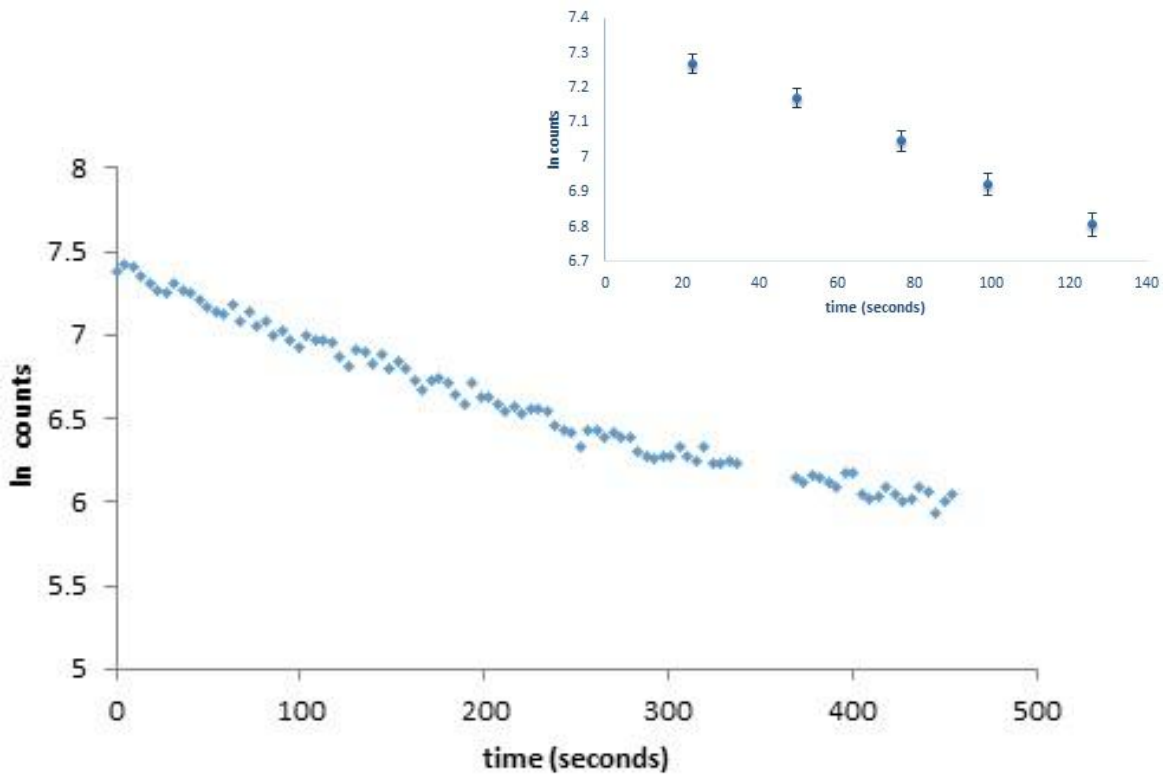


**Fig. 3-6.** Decay of activity from the sample of bone irradiated with 25 MV beam of photons, with the inset showing error bars (random error in the counts) for a few typical data points.

Figures 3-5 and 3-6 show the background subtracted decay of activity with time from a sample of bone irradiated with a 25 MV beam of photons, on a linear and semi-log scale respectively. The exponential ( $y = 1425.6e^{-0.0048x} + 209$ ) and linear graphs ( $y = -0.0048x + 7.21$ ) give a decay constant of 0.0048 per second, which corresponds to a half-life of 2.4 minutes.

The half-life measured by decay of activity (in the time mode of the analyzer) differs from that measured by the decay of 511 KeV photons (in the energy mode of the analyzer) by about 16%. The decay of 511 KeV photons was counted with the analyzer in the energy mode for about 150 seconds (figures 3-3 and 3-4) while the decay of activity was counted with the analyzer in the time mode for roughly 500 seconds (figures 3-5 and 3-6). The counting time for the energy mode was too short for the measured half-life to be influenced by any competing decay of half-life longer than the measured 122 seconds. The counting time for the time mode was long enough for a competing decay of longer half-life to influence the measured half-life.

The presence of  $^{12}\text{C}$  in the samples irradiated accounts for the competing decay of  $^{11}\text{C}$  from the  $^{12}\text{C}(\gamma, n)^{11}\text{C}$  reaction.  $^{11}\text{C}$  decays with a half-life of 20.1 minutes<sup>13</sup>, the influence of which can be seen as an increase in the measured half-life from the sample that was counted for about 8 minutes, compared to that which was measured from the sample that was counted for about 2.5 minutes. In experiments done to study tumor blood flow by measuring positron activity, it had been found that beyond ten minutes post activation,  $^{11}\text{C}$  becomes the major source of activity from the activated sample.<sup>38</sup>

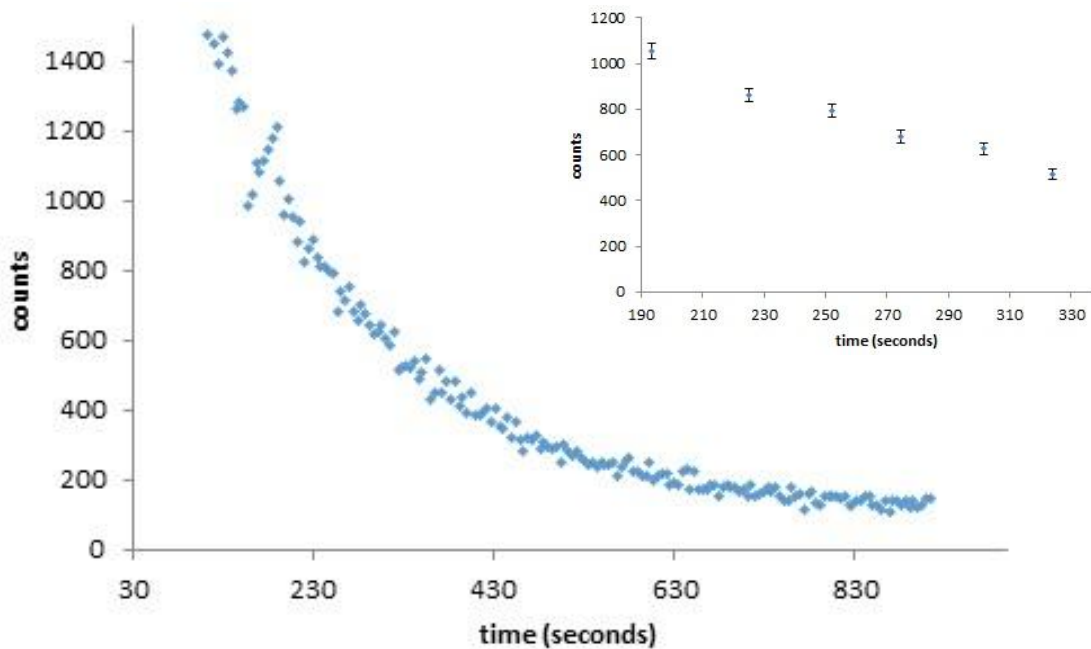


**Fig. 3-7.** Decay of activity from a sample of bone irradiated by an 18 MV beam of photons. The inset shows a few typical points with error bars (random error in the counts).

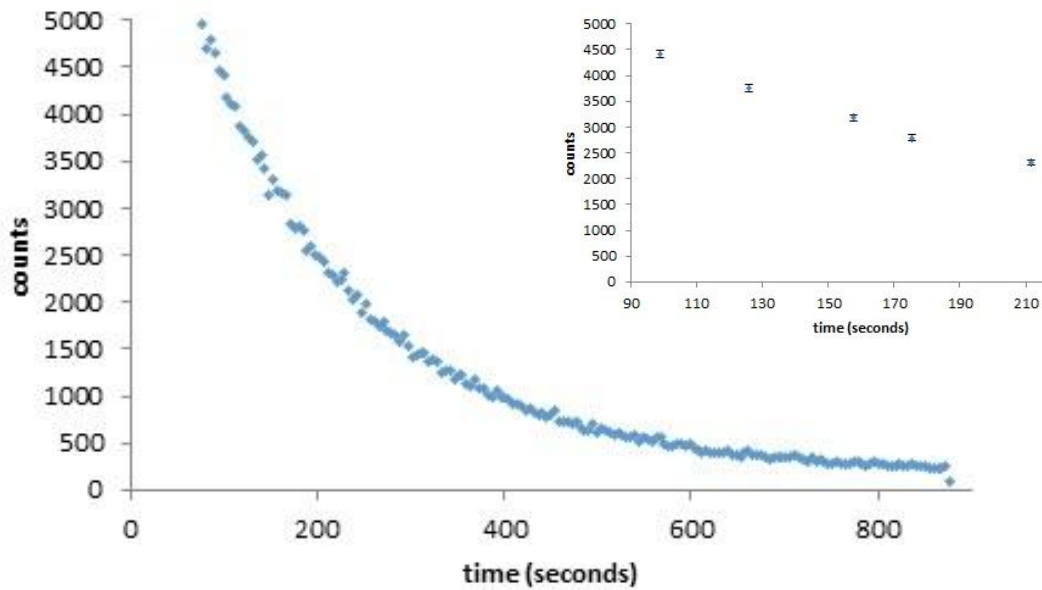


**Fig. 3-8.** Decay of activity from a sample of tissue irradiated by an 18 MV photon beam. The inset shows error bars (random error) for a few typical points.

Figures 3-7 and 3-8 show the decay of activity measured from a sample of bone and a sample of tissue respectively, irradiated by an 18 MV beam of photons for roughly 19 minutes.

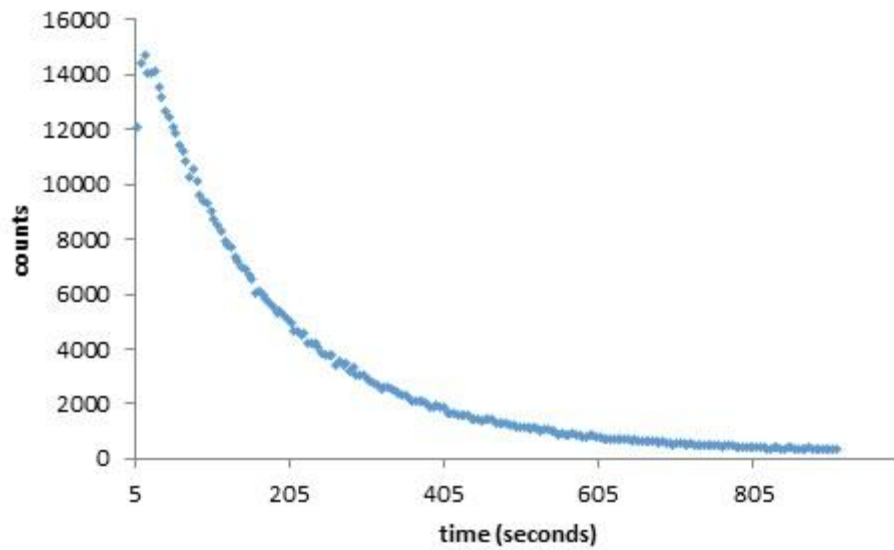


**Fig. 3-9.** Decay of activity as seen from a bone surrounded by tissue after being irradiated with 18 MV photons. Error bars showing the random in the number of counts are not visible in the scale of the Y-axis.

Figure 3-9 shows the decay of activity measured from a sample of bone surrounded by tissue irradiated by an 18 MV beam of photons for about 19 minutes.

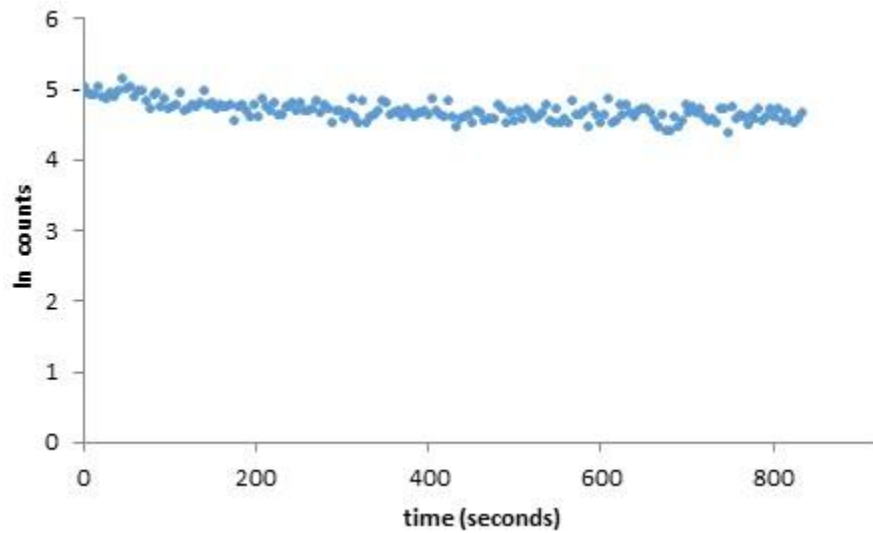
The decays shown in the figures 3-8 ( $y = 6759.9e^{-0.005x}$ ) and 3-9 ( $y = 14295e^{-0.005x}$ ) yield a half-life of 2.3 minutes. This half-life is comparable to what was measured using a sample of bone activated by 25 MV photons, as shown in figure 3-5. This is also 16% higher than the half-life measured from figures 3-3 and 4 due to the decay of  $^{11}\text{C}$  with a longer (20.1 minutes) half-life.

Figure 3-7 ( $y = 2409.4e^{-0.0043x}$ ) yields a higher half-life of 2.7 minutes. The sample of bone had to be adjusted in the holder during the counting. The trial was not repeated as the sample was already activated.

### 3.2 Result

As seen above, the measured half-lives correspond to the decay of  $^{15}\text{O}$  resulting from the  $^{16}\text{O}(\gamma, n)^{15}\text{O}$  reaction.

The following figure (3-10) shows the measured activity of 99.99% pure calcium irradiated by 18 MV photons. No decay of significance was observed due to the delay in starting the analysis of decay of 511 KeV photons. As discussed in sections 2.2.5 and 2.3, the irradiated sample had to be manually transported for the decay products to be analyzed. The transit time of minimum 20 seconds meant not being able to observe the decay of the shorter half-life of 0.9 seconds for calcium.



**Fig. 3-10.** Measured activity from a sample of 99.99% calcium after being irradiated by an 18 MV beam.

The duration of the counting time was not long enough to measure the decay rate of  $^{11}\text{C}$ , as the counts from the sample were not distinguishable from those of the background past eight or nine minutes.



## Chapter 4

### Discussion

#### 4.1 Energy of the incident photons

The spectrum of a megavoltage photon beam is that of bremsstrahlung emission produced by thick targets and filtered by flattening filters and shaped by collimators. The maximum photon energy is equal to the maximum incident electron energy. The photon fluence increases with decreasing energy typically reaching a peak at an energy about one-third of the maximum. At energies lower than at the peak, fluence decreases due to the attenuation of low energy photons by the target material.<sup>39</sup>

Direct measurement of photon energy distribution of the bremsstrahlung spectrum is not feasible due to the high fluence of the high energy photon beams saturating the detectors and the challenge of determining detector efficiency for high-energy photons. Photon fluence information in clinically used photon beams is helpful for accurate dose calculations especially around tissue interfaces and inhomogeneity, for accurate modelling of energy response of various detectors, and also for better design of treatment head and flattening filter.<sup>40</sup>

In the kilo voltage energy range, the total attenuation coefficient is steeply decreasing due to the dominance of photoelectric interaction (refer figure 1-4) which allows for a good differentiation between successive energy intervals. However, in the megavoltage energy range, the slowly decreasing Compton cross section and the increasing contribution of pair production cross section to the total attenuation coefficient leads to reduction in energy differentiation, making the task of deriving the spectra more demanding on the method employed.<sup>41</sup> Various methods that estimate the energy distribution include estimating the spectrum by matching measured depth-dose,<sup>42</sup> attenuation or transmission analysis,<sup>42,43</sup> Laplace transform,<sup>44</sup> Monte Carlo simulation, etc.

Currently, Monte Carlo simulation remains the most comprehensive and potentially more accurate method to estimate the energy distribution of photons in a clinical beam.<sup>45,46</sup> The accuracy of Monte Carlo simulation is limited to the modelling of the treatment head and assumptions made concerning the electron beam incident on the target.<sup>41</sup> The information on the design of the treatment head is difficult to obtain from competing manufacturers. Also, with constantly improving accelerator designs, even within a given model, machines are often adjusted for individual purchasers to match previous beam characteristics.<sup>47</sup>

The photon fluence information available from the Monte Carlo simulation using BEAM code<sup>45,46</sup> has been used for the purposes of calculating interaction probabilities for the activation of the observed reaction.

## 4.2 Interaction cross-section for the observed reaction

The threshold for this interaction, as seen from figures 1-6 and 1-7 for the  $O^{16}(\gamma,n)O^{15}$  reaction is 15.5 MeV. The reaction has resonances at various higher energies with a maximum cross section of 15 milli barns around 22 MeV. At the energy of the photons that are available in the bremsstrahlung beam to initiate the reaction, the reaction had a cross-section of  $1.25 \times 10^{-29} \text{ cm}^2 / \text{atom}$ .

The neutrons released in this reaction are high-ranged particles and deposit dose outside of the sample. The positrons, being charged particles deposit dose along their track, before annihilating with an electron to produce two photons of 511 KeV each.

## 4.3 Dose due to the positrons released

The deposition of energy by moving charged particles is mainly a result of a series of electric field interactions that occur at random along its track. The particle's energy loss  $-dE$ , along a portion of its track  $dx$ , is dependent on its velocity  $v$ , charge  $Z$ , and the electron density of the target  $\rho$ .<sup>48</sup>

$$-dE/dx \propto Z^2 \rho / v^2$$

### 4.3.1 The range of the positrons

Electrons and positrons follow a tortuous path in matter due to elastic and inelastic scattering by atomic nuclei and electrons. In the energy range of  $10^4$  eV to  $10^7$  eV, the difference between energy loss and multiple scattering of positrons and electrons is insignificant.<sup>49</sup>

In this energy range, their deflection in matter is due almost entirely to the elastic collisions with atomic nuclei<sup>49</sup>, with an interaction probability that is proportional to the square of atomic number of the medium ( $Z^2$ ) approximately to  $1/E^2$  where E is the kinetic energy of the incident positrons. The scatter angle is inversely proportional to the energy of the positrons. Energy loss due to Bremsstrahlung in the Coulomb field of the nucleus is negligible.

Their energy loss is primarily from inelastic interactions with atomic electrons, where the incident electron loses energy and gets deflected at some angle with respect to the original. This interaction probability increases with the atomic number of the medium and decreases rapidly with increasing kinetic energy of the incident positrons.<sup>50</sup> The energy transferred to the atoms per collision is very small. The total energy loss after passage through a given thickness of matter is therefore the result of a very large number of small energy losses.<sup>49</sup>

The range of the positrons is defined as the penetration depth (a straight line path) which can be identified by statistical distribution parameters like full width at half-maximum (FWHM).<sup>51</sup> The average energy lost per distance ( $dE/dx$ ) traversed by an ionizing particle in a material made of independent atoms and due only to inelastic processes (ionization and excitation) has been given by the Bethe–Bloch formula\*.

The value for  $dE/dx$  rapidly increases as the positron slows down and therefore most of the ionization created in an electron track will be towards the end.

Thus, at the beginning of the track (at higher energies), scatter at small angles is dominant. As the positron slows down toward the end of its trajectory, scattering at large angles becomes more frequent, and energy loss,  $dE/dx$  increases rapidly.<sup>49</sup>

Therefore most of the ionization created in an electron/positron track will be towards the end.

Therefore, it is pertinent to use pathlength,  $l$  obtained by using the continuous slowing down approximation range, given by the integral of the reciprocal of the stopping power

---

\*  $dE/dx = 4\pi r_0^2 (mc^2/\beta^2) N Z (A + B)$

where  $A = \ln [ \beta\gamma \sqrt{(\gamma-1) mc^2 / I} ]$

$$B = 1 / (2\gamma^2) \{ [(\gamma-1)^2 / 8] + 1 - (2\gamma^2 + 2\gamma - 1) \ln 2 \}$$

$$\gamma = 1/\sqrt{1-\beta^2}$$

$N$  is the number density of atoms in the medium

$r_0$  is the classical electron radius, and

$I$  (eV) is the average excitation potential of the medium.

of the medium (until the velocity of the particle falls to a value comparable to that of atomic electrons) for dose considerations.

$$l(T) = \int_0^T \left[ \frac{1}{\rho} \left( \frac{dE}{dx} \right) \right]^{-1} dT$$

where  $1/\rho (dE/dx)$  is the stopping power of the medium and  $T$  is the kinetic energy of the positrons.

Experiments<sup>52,53</sup> have shown the average range of the positrons to be 8 mm and 5 mm in muscle (soft tissue and body fluids) and in bone respectively for a maximum energy of 1.7 MeV. For an average energy of 0.7 MeV, the average range has been measured to be 2.8 mm in muscle and 1.7 mm in bone.

Given the short range of positrons, it can be assumed that the energy absorbed by the medium is equal to the energy released in it by the positrons.

#### **4.4.2 Linear Energy Transfer of the positrons**

Linear energy transfer (LET) is the average energy lost by the particle over a given path length. It depends on the velocity and hence, the energy and the charge of the particle.<sup>54</sup> When the charged particle has its full energy, LET is small. As the particle loses energy more rapidly toward the end of its range, it reaches a maximum rate of energy loss, also known as the Bragg peak, just before it comes to rest. The LET of the particle, therefore, varies along the length of its range.

Due to the multiple deflections that it goes through as it slows down, the Bragg peak (a sharp and significant increase in the energy deposited at the end of the track) is not observed for positrons.<sup>54</sup> The positron has an increased energy loss,  $dE/dx$  at its termination, and a range of LET values along its path. But, since the initiation (following an irradiation with photons) and termination of the positron tracks occur at random in the tissue, the LET spectrum is similar at all depths.<sup>55</sup>

The end-point energy of 1.7 MeV of the positrons corresponds to a linear energy transfer of 0.188 KeV/ $\mu\text{m}$  in muscle and 0.174 KeV/ $\mu\text{m}$  in bone. The LET of positrons with an average energy of 0.7 MeV is 0.193 KeV/ $\mu\text{m}$  in muscle and 0.1799 KeV/ $\mu\text{m}$  in bone.<sup>56</sup>

### **4.3.3 Measured local dose enhancement due to positrons**

As mentioned in section 2.2.3, the detector was calibrated with a radioactive source of Na-22 of known activity at various positions along the length of the bone holder. Averaged over the length of the bone, the detector was found to detect 10% of the radiation emitted. The positron emission following the ( $\gamma, n$ ) reaction is delayed (not prompt). As the direction of positron emission from the vibrating nucleus is not correlated to the direction of the photon's incidence, the positrons are emitted isotropically. The duration of the photon flux was also of short enough duration compared to that of the measured half-life.

Assuming the positrons to deposit dose in a sphere of radius equal to their range (with the spheres overlapping), the dose deposited per positron in bone was found to be  $1.97 \times 10^{-9}$  Gray\*. With the number of positrons as estimated by the counts of 511 KeV photons detected, the dose deposited by the positrons in bone was found to be 0.18 milli Gray for an externally delivered dose of 13 Gray. (Refer to Appendix 1)

Similarly, the dose deposited per positron in tissue was found to be  $1.22 \times 10^{-9}$  Gray. With the estimated total number of positrons emitted, the dose deposited by the positrons in the sample of tissue was found to be 0.025 mGy for an externally delivered dose of 13 Gray. (Refer to Appendix 2).

The bone was assumed to be a cylinder of radius 0.6 cm. The attenuation of 511 KeV photons by the sample has been considered to be negligible in this calculation.

The dose enhancement in the sample of bone was found to be about seven times higher than that in the sample of tissue.

The ratio of oxygen to other elements in bone is higher than that of tissue. A form of apatite with most of the OH groups being replaced by many carbonate and phosphate substitutions is a large component (up to 70% by weight) of bone material\*\*.

---

\* 1 Gray = 1 Joule/Kilogram

\*\*  $\text{Ca}_5(\text{PO}_4)_3(\text{F},\text{Cl},\text{OH})$



This measured enhancement of dose is due to positrons from the decay of the  $^{15}\text{O}$  which was a product of the  $^{16}\text{O}(\gamma,n)^{15}\text{O}$  reaction. This measurement does not include the dose delivered locally by positrons emitted promptly due to pair production while the beam was on.

#### **4.4 Thermoluminescent dosimeters**

Thermoluminescent dosimeters (TLD) give a measure of absorbed dose at the site of insertion. They measure dose due to both primary and secondary charged particles. The results of this measurement are not sufficient to measure the dose delivered by positrons alone in tissue and in bone.

## Chapter 5

### Conclusion

#### 5.1 Measured dose enhancement

To the accuracy of the calculations, the measured dose enhancement from the recoil energy of positrons in bone was 0.002% of the externally delivered dose. In tissue, it was measured to be 0.00031% of the dose delivered externally. This measurement was from the spectrum obtained from the activated samples. Thermoluminescent dosimeters and photochromic films are not sensitive enough to measure this enhancement over the externally delivered dose.

##### 5.1.1 Expected positron yield

From figure 1-6, the reaction has a cross section of  $1.25 \times 10^{-29} \text{ cm}^2/\text{atom}$  at the range of photon energies that was available in the bremsstrahlung beam. Using the simulation information from reference 45, about 1.3% of the incident photon beam was of the energy that could initiate the  $^{16}\text{O}(\gamma, n)^{15}\text{O}$  reaction.

Assuming the bone to be a cylinder, using the average volumes of the circumscribed and inscribed cuboids, the number of oxygen atoms in the sample was estimated. As the sample was not of crystalline form where the atoms are arranged in lines, and also due to the small thickness of the sample, it can be assumed that there was no hiding of the

atoms. As the cross-section was of the order of  $10^{-29} \text{ cm}^2$ , it can be assumed that the absorption of photons was the same in every layer of atoms. The expected yield of positrons from  $(\gamma, n)$  reaction was estimated to be of the order of  $10^5$  to  $10^6$  in magnitude. (Appendix 3). The measurement using the spectrum of activated samples yielded positrons of order of  $10^5$  in bone, as shown in appendix 1.

The interaction cross-section for the reaction and number of photons available in the incident beam of energy needed to initiate the reaction are small. The highest measured cross section for the reaction is 15 milli barn at 22 MeV. Enhancing the reaction offers the possibility of introducing excited oxygen atoms and hence secondary charged particles (positrons) into the irradiated region, in addition to the primary electrons and positrons released due to the interaction of the incident photons with the irradiated matter.

## **5.2 Enhancing the reaction in a high energy linear accelerator**

As the photo-activation of  $^{15}\text{O}$  is most effective at energies between 20 and 30 MeV<sup>57</sup>, the  $^{16}\text{O} (\gamma, n)^{15}\text{O}$  reaction can be enhanced by choosing the energy of the incident photons appropriately.

### 5.2.1 Filter to absorb lower end of Bremsstrahlung

The  $^{16}\text{O}(\gamma,n)^{15}\text{O}$  reaction has a threshold energy of 15.5 MeV. As mentioned in section 2.1.1, the lower energy photons (in the Bremsstrahlung spectrum and Compton scattered photons) do not contribute toward activating the desired reaction, but toward the externally delivered photon dose and hence not to the dose enhancement. The apparent probability of the reaction for a given total flux of photons can be enhanced by removing the lower energy photons from the beam incident on the sample.

Experiments done for studying perfusion imaging using *in situ*  $^{16}\text{O}(\gamma,n)^{15}\text{O}$  activation have used a 12 cm thick carbon block to preferentially absorb the lower energy photons in the beam in order to achieve this desired result.<sup>58</sup>

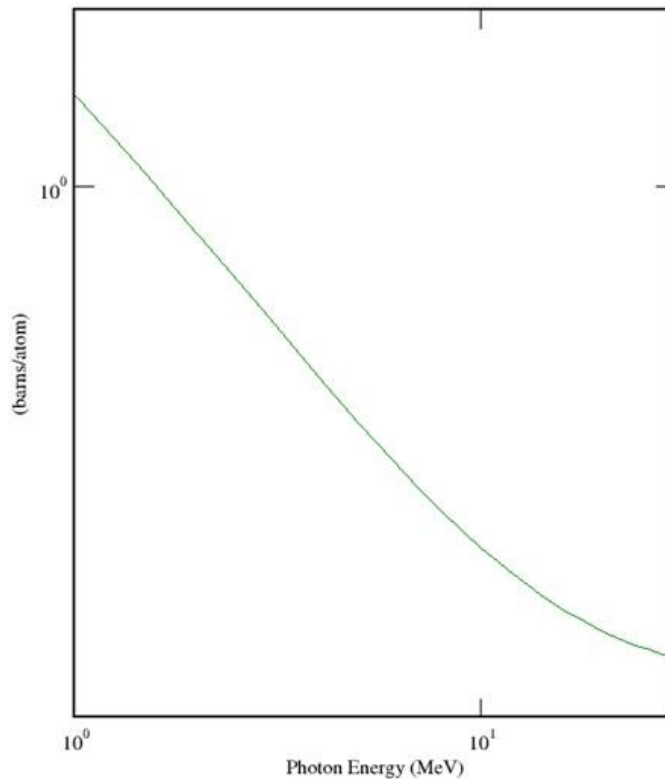


**Fig. 5-1.** Total photon attenuation cross-section in Carbon as a function of photon energy<sup>58</sup>

As seen from figure 5-1, low atomic number materials like carbon have a higher cross section at lower photon energies compared to that at higher energy. Carbon has a cross-section of 1.3 barns/atom at MeV and 0.31 barns/atom at 20 MeV. The high cross-section at lower energy and the decreasing cross-section with increasing energy (within the energy range of 1 MeV to 30 MeV) is conducive to absorbing lower energy photons from the Bremsstrahlung spectrum.

### **5.2.2 Neutron contamination in a high energy linear accelerator**

When the incident photon beam contains photons of energy 8 MeV or higher, ( $\gamma,n$ ) and ( $e,n$ ) reactions are initiated. The photo-neutrons are generated mainly when the photons interact with the high atomic number materials in the components (bremsstrahlung target, filters, jaws, etc.) of accelerator itself<sup>59</sup>. The neutrons react with elements in the patient, floor, ceiling and walls of the room and are of higher radio biological effectiveness than that of photons. It has been found that neutrons in a typical treatment room are of energy ranging from 0.1 MeV to 10 MeV coming from the accelerator head, and of energy less than 0.1 MeV when they are scattered.<sup>60</sup> Neutrons of energy 2.5 MeV have a LET (linear energy transfer) of 15-80 KeV/ $\mu\text{m}$  and that of energy 14 MeV have a LET of 3-30 KeV/ $\mu\text{m}$ .<sup>61</sup> Monitoring neutron production and neutron shielding becomes a necessity when the accelerator is being operated at high (10 or above) mega voltages.

### **5.3 Enhancing the reaction by using quasi monoenergetic beams**

The dose enhancing reaction can be maximized by choosing the energy of the incoming photons to be within 20 and 30 MeV. Quasi monoenergetic photon beams are an attractive option as the reaction has high cross-sections at certain energies, as seen from figure 1-6. Photons from radioactive sources and charged particle reactions are of discrete energy but are usually of low intensity and also are not of variable energy.

#### **5.3.1 Annihilation in flight of monoenergetic fast positrons**

Positrons of thermal energy produce two 511 KeV photons as they annihilate with an electron. If the positron annihilates while in flight, its kinetic energy is imparted to the annihilation photons. By choosing the velocity of the positrons appropriately, the annihilation photons can be of the desired energy within a small range.

The positrons produced by pair production from an electron linear accelerator are magnetically selected for velocity to give a beam of nearly monoenergetic positrons. These positrons, when made to strike a low atomic number target annihilate in flight. As momentum is conserved at small angles, it is possible to produce a beam of nearly monochromatic photons in the forward direction. By varying the energy of the positrons, this photon beam can be made variable in energy. Photon energy resolution of about 3% has been achieved using this method.<sup>62</sup>

## 5.4 Conclusion

The dose delivered by secondary charged particles from the photo nuclear disintegrations that occur in the range of energies available in bremsstrahlung spectrum of photons was attempted to measure to explore the feasibility of local dose enhancement due to photo nuclear disintegrations.

The predominant photo nuclear interaction that was measured in the range of photon energies available in the bremsstrahlung spectrum seems to be the  $^{16}\text{O}(\gamma,n)^{15}\text{O}$  reaction. The giant dipole resonance of calcium in bone could not be measured against the heavy background due to its short half-life.

The measured dose enhancement in bone and in tissue due to the  $^{16}\text{O}(\gamma,n)^{15}\text{O}$  reaction was a small percentage of the externally delivered dose. The dose enhancement due the photo nuclear reactions can be exploited to be of clinical significance by selectively choosing the energy of the incident beam to be predominantly of 20 – 30 MeV.

## Reference

1. R.E. Lapp, H.L. Andrews, "Nuclear Radiation Physics", Engelwood Cliffs : Prentice-Hall, 1948; 237.
2. F.M. Khan, "The Physics of Radiation Therapy", Lippincott Williams & Wilkins, 2003; 66.
3. F. M. Khan, "The Physics of Radiation Therapy", Lippincott Williams & Wilkins, 2003; 72.
4. Scattering of X-rays from electrons and atoms, <http://xdb.lbl.gov/Section3> (Date accessed : April 4, 2016).
5. R.E. Lapp, H.L. Andrews, "Nuclear Radiation Physics", Engelwood Cliffs : Prentice-Hall, 1948; 291.
6. C.M. Lederer, V.S. Shirley (editors), "Table of Isotopes" 7<sup>th</sup> edition. Wiley-Interscience, 1978, p. 17.
7. J. Mantel, "The Beta ray spectrum and the average beta energy of several isotopes of interest in medicine and biology," *International Journal of applied radiation and isotopes* **23**, 407-413 (1972).
8. B.C. Cook, J.E.E. Baglin, J.N. Bradford, J.E. Griffin, " $O^{16}(\gamma,n)O^{15}$  Cross section from threshold to 65 MeV", *Physical Review* **143-3**, 712-723 (1965).
9. M.N. Martins, V.P. Likhachev, J.D.T. Arruda-Neto, R. Guarino, F. Gerab, "Tagged bremsstrahlung polarization : a Monte-Carlo approach", *Nuclear Instruments and Methods in Physics Research A* **390**, 375-382 (1997).
10. V.P. Likhachev, M.N. Martins, M.T.F. da Cruz, L.C. Maximon, "Geometrical selection of a quasi-monochromatic, linearly polarized component of the bremsstrahlung spectrum", *Nuclear Instruments and Methods in Physics Research A* **457**, 415-418 (2001).
11. S.S. Dietrich, B.L. Berman, "Atlas of photoneutron cross sections obtained with monoenergetic photons", *Atomic data and Nuclear data tables* **38**, 199-338 (1988).



12. M. Oldham, S.A. Sapareto, X.A. Li, S. Sutlief, O.C. Wong, J.W. Wong, "Practical aspects of in situ  $O^{16}(\gamma,n)O^{15}$  activation using a conventional medical accelerator for the purpose of perfusion imaging", *Medical Physics* **28(8)**, 1669-1878 (2001).
13. C.M. Lederer, V.S. Shirley (editors), "Table of Isotopes" 7<sup>th</sup> edition. Wiley-Interscience, 1978, p. 8.
14. A. Bohr, B.R. Mottleson, "Nuclear Structure", Reading : W.A. Benjamin, Inc., 1975; 476.
15. C.M. Lederer, V.S. Shirley (editors), "Table of Isotopes" 7<sup>th</sup> edition. Wiley-Interscience, 1978, p. 86.
16. G.L. Locher, "Biological effects and therapeutic possibilities of neutrons," *Am J Roentgenol and Radium Therapy* **36**, 1-13 (1936).
17. H. W. Schmitt, R.C. Block, R. L. Bailey, "Total neutron cross section of  $^{10}B$  in the thermal neutron energy range," Oak Ridge National Laboratory, Tennessee, 1959.
18. H. Tokumitsu, J. Hiratsuka, Y. Sakurai, T. Kobayashi, H. Ichikawa, Y. Fukumori, "Gadolinium neutron-capture therapy using novel gadopentetic acid-chitosan complex nanoparticles: in vivo growth suppression of experimental melanoma solid tumor," *Cancer Letters* **150**, 177-182 (2000).
19. J.A. Shih, R.M. Brugger, "Gadolinium as a neutron capture agent," *Medical Physics* **19**, 733 (1992).
20. C. Salt, A.J. Lennox, M. Takagaki, J.A. Maguire, N.S. Hosmane, "Boron and Gadolinium neutron capture therapy," *Russian Chemical Bulletin International Edition* **53-9**, 1871-1888 (2004).
21. M.J. Luderer, P. Puente, A.K. Azab, "Advancements in tumor targeting strategies for Boron neutron capture therapy," *Pharm Res* **32**, 2824-2836 (2015).
22. D. Yoon, J. Jung, K.J. Hong, T.S. Suh, "Tomographic image of prompt gamma ray from boron neutron capture therapy: A Monte Carlo simulation study," *Applied Physics Letters* **104**, 083521 (2014).
23. M.H. Castillo, T.M. Button, R. Doerr, M.I. Homs, C.W. Pruett, J.I. Pearce, "Effects of radiotherapy on mandibular reconstruction plates," *The American Journal of Surgery* **156**, 261-263 (1988).
24. S.J. McMahon, M.H. Mendenhall, S. Jain, F. Currell, "Radiotherapy in the presence of contrast agents: a general figure of merit and its applications to gold nanoparticles," *Phys. Med. Biol.* **53**, 5635-5651 (2008).

25. K.T. Butterworth, J.A. Coulter, S. Jain, J. Forker, S.J. McMahon, G. Schettino, K.M. Prise, F.J. Currell, D.G. Hirst, "Evaluation of cytotoxicity and radiation enhancement using 1.9 nm gold particles: potential application for cancer therapy," *Nanotechnology* **21**, 295101 (2010).
26. K.T. Butterworth, S.J. McMahon, F.J. Currell, K.M. Prise, "Physical basis and biological mechanisms of gold nanoparticle radiosensitization," *Nanoscale* **4**, 4830 (2012).
27. C.S. Cutler, H.M. Hennkens, N. Sisay, S. Huclier-Markai, S.S. Jurisson, "Radiometals for combined imaging and therapy," *Chem. Rev.* **113**, 858–883 (2013).
28. J.F. Hainfield, D.N. Slatkin, H.M. Smilozitz, "The use of gold nanoparticles to enhance radiotherapy in mice," *Phys. Med. Biol.* **49**, N309-N315 (2004).
29. W.N. Rahman, N. Bishara, T. Ackerly, C.F. He, P. Jackson, C. Wong, R. Davidson, M. Geso, "Enhancement of radiation effects by gold nanoparticles for superficial radiation therapy," *Nanomedicine: Nanotechnology, Biology, and Medicine* **5**, 136-142 (2009).
30. D.G. Zhang, V. Feygelman, E.G. Moros, K. Latifi, G.G. Zhang, "Monte Carlo study of radiation dose enhancement by Gadolinium in megavoltage and high dose radiotherapy," *PLoS ONE* **9**, Issue 10 (2014).
31. A. Alkhatib, Y. Watanabe, J.H. Broadhurst, "The local enhancement of radiation dose from photons of MeV energies obtained by introducing materials of high atomic number into the treatment region," *J Med. Phys.* **36(8)** (2009).
32. M. Estorch, I. Carrio, "Future challenges of multi-modality imaging," *Recent Results in Cancer Research* **187**, 403-415 (2013).
33. M. Hamoudeh, M.A. Kamleh, R. Diab, H. Fessi, "Radionuclides delivery systems for nuclear imaging and radiotherapy of cancer," *Advanced Drug Delivery Reviews* **60**, 1329-1346 (2008).
34. R. R. Raylman, R.L. Wahl, "Magnetically enhanced radionuclide therapy," *J Nucl. Med.* **35**, 157-163 (1994).
35. R. Zimmermann, "Nuclear Medicine – Radioactivity for Diagnosis and Therapy," *EDP Sciences, France*, 2007; 84).
36. Df R.K. Hobbie, B.J. Roth, "Intermediate Physics for Medicine and Biology", Springer, 2007; 463.

37. Photon attenuation cross-section, [www.physics.nist.gov](http://www.physics.nist.gov) (Date last accessed : August 6, 2016).
38. R. K. Ten Haken, G.H. Nussbaum, B. Emami, W.L. Hughes, "Photon activation-<sup>15</sup>O decay studies of tumor blood flow," *Journal of Medical Physics* **8(3)**, 324-336 (1981).
39. P. Metcalfe, T. Kron, P. Hoban, "The Physics of Radiotherapy X-rays and electrons", Madison : Medical Physics Publishing, 2007; 76.
40. P. Francoise, F. Coste, J. Bonnet, O. Caselles, "Validation of reconstructed bremsstrahlung spectra between 6MV and 25MV from measured transmission data", *Medical Physics* **24**, 769-773 (1997).
41. C.R. Baker, B. Ama'ee, N.M. Spyrou, "Reconstruction of megavoltage photon spectra by attenuation analysis", *Physics in Medicine and Biology* **40**, 529-542 (1995).
42. E.S.M. Ali, D.W. O. Rogers, "An improved physics-based approach for unfolding megavoltage bremsstrahlung spectra using transmission analysis", *Medical Physics* **39**, 1663-1675 (2012).
43. R.G. Waggner, M.M. Blough, J.A. Terry, D. Chen, N.E. Lee, S. Zhang, W.D. McDavid, "X-ray spectra estimation using attenuation measurements from 25kVp to 18 MV", *Medical Physics* **26**, 1269-1278 (1999).
44. R. Archer, P.R. Almond, L.K. Wagner, "Application of a Laplace transform pair model for high-energy x-ray spectral reconstruction", *Medical Physics* **12**, 630-633 (1985).
45. D.W.O. Rogers, B.A. Faddegon, G.X. Ding, C.M. Ma, J. We, T.R. Mackie, "BEAM: A Monte Carlo code to simulate radiotherapy treatment units", *Medical Physics* **22**, 503-524 (1995).
46. D. Sheikh-Bagheri, D.W.O. Rogers, "Monte Carlo simulation of nine megavoltage photon beam spectra using the BEAM code" *Medical Physics* **29**, 391-402 (2002).
47. A. Nisbet, H. Weatherburn, J.D. Fenwick, G. Mc Vey, "Spectral reconstruction of clinical megavoltage photon beams and the implications of spectral determination of the dosimetry of such beams", *Physics in Medicine and Biology* **43**, 1507-1521 (1998).
48. I. F. Tannock, R.P. Hill, "The Basic Science of Oncology," 3<sup>rd</sup> edition. McGraw-Hill, 1998. p. 297.

49. C.S. Levin, E.J. Hoffman, "Calculation of positron range and its effect on the fundamental limit of positron emission tomography system spatial resolution," *Physics in Medicine and Biology* **44**, 781-799 (1999).
50. W.R. Hendee, E.R. Ritenour, "Medical Imaging Physics," 4<sup>th</sup> edition. New York : Wiley-Liss Inc., 2002, p.49.
51. M. E. Phelps, E.J. Hoffman, S.C. Huang, M.M. Ter-Pogossian, "Effect of positron range on spatial resolution," *Journal of Nuclear Medicine* **16** (7), 649-652 (1975).
52. Z. H. Cho, J. K. Chan, L. Ericksson, M. Singh, S. Graham, N. S. MacDonald, Y. Vano, "Positron ranges obtained from biomedically important positron-emitting radionuclides," *Journal of Nuclear Medicine* **16**, 1174-1176 (1975).
53. M.J. Berger, S.M. Seltzer, "Table of energy losses and ranges of electrons and positrons" National Aeronautics and Space Administration, Washington, 1964.
54. M. E. Johns, J.R. Cunningham, "The Physics of Radiology," 4<sup>th</sup> edition. Thomas Books, Springfield, Illinois, 1983, p.213.
55. I.F. Tannock, R.P. Hill, "The Basic Science of Oncology," 3<sup>rd</sup> edition. McGraw-Hill, 1998, p. 298.
56. M.J. Berger, S.M. Seltzer, "Table of energy losses and ranges of electrons and positrons" National Aeronautics and Space Administration, Washington, 1964.
57. M. Oldham, S.A. Sapareto, X.A. Li, J. Allen, S. Sutlief, O.C. Wong, W.J. Wong, "Practical aspects of in situ  $^{16}\text{O}$  ( $\gamma, n$ )  $^{15}\text{O}$  activation using a conventional medical accelerator for the purpose of perfusion imaging," *Medical Physics* **28**, 1669-1678 (2001).
58. Photon attenuation cross-section, [www.physics.nist.gov](http://www.physics.nist.gov) (Date last accessed: August 6, 2016).
59. K. Amgarou, V. Lacoste, A. Martin, "Experimental characterization of the neutron spectra generated by a high-energy clinical LINAC", *Nuclear Instruments and Methods in Physics Research A* **629**, 329-336 (2011).
60. F. Gomez, A. Iglesias, F.S. Doblado, "A new active method for the measurement of slow-neutron fluence in modern radiotherapy treatment rooms", *Physics in Medicine and Biology* **55**, 1025-1039 (2010).

61. I.F. Tannock, R.P. Hill, "The Basic Science of Oncology," 3<sup>rd</sup> edition. McGraw-Hill, 1998, p. 297.
62. S.C. Fultz, R.L. Bramblett, J.T. Caldwell, NA. Kerr, "Photon cross-section measurements on gold using nearly monochromatic photons," Physical Review **127-4**, 1273-1279 (1962).

## Appendix 1

Average range of a positron of recoil energy 0.7 MeV in bone = 1.7mm

Volume of a sphere of bone, of radius 1.7 mm =  $2.058 \times 10^{-8} \text{ m}^3$

Therefore, on an average, energy of 0.7 MeV is deposited within this sphere of bone.  
(i.e)  $1.12 \times 10^{-13}$  Joules of energy is deposited per positron within this sphere of bone.

Taking the density of bone to be  $1900 \text{ Kg/m}^3$ ,  
mass of the sphere of bone under consideration =  $3.9 \times 10^{-5} \text{ Kg}$ .

Dose delivered to this mass =  $2.87 \times 10^{-9}$  Gray/positron.

The decay equation of figure 3-4 (shown below) gives an estimate of 511 KeV photons detected from the positron decay. Each positron decay resulted in the emission of two 511 KeV photons. The detector detected 10% of what was emitted into  $4\pi$  steradians. The estimated number of positrons released after the irradiation =  $91,440 \pm 675$ .

Total dose delivered in the sample of bone by the recoil energy of positrons released in it =  $0.26 \pm 0.0013 \text{ mGy}$ .

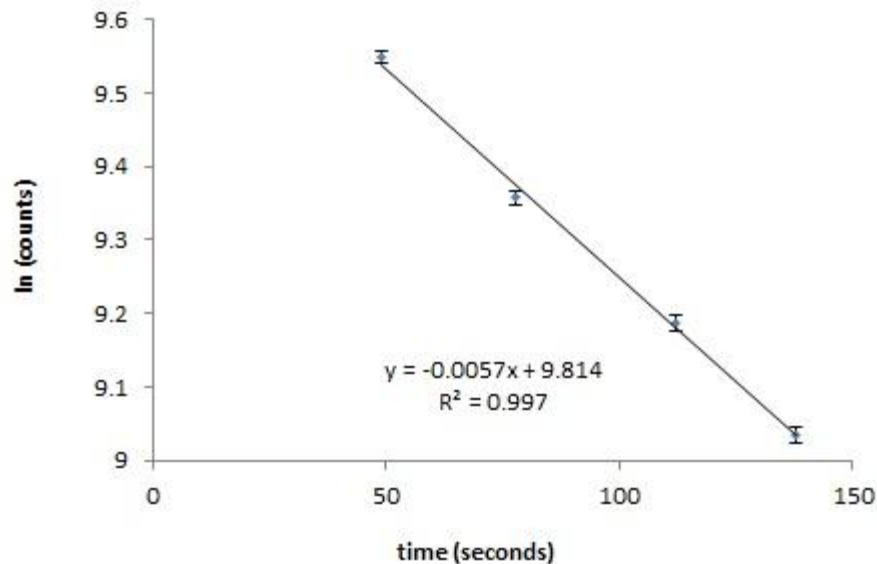


**Fig. 3-4.** Decay of 511 KeV photons with time as measured from an activated sample of bone.

## Appendix 2

Average range of a positron of recoil energy 0.7 MeV in tissue = 2.8mm

Volume of a sphere of tissue, of radius 2.8 mm =  $9.195 \times 10^{-8} \text{ m}^3$

Therefore, on an average, energy of 0.7 MeV is deposited within this sphere of bone.  
(i.e)  $1.12 \times 10^{-13}$  Joules of energy is deposited per positron within this sphere of tissue.

Taking the density of tissue to be  $1000 \text{ Kg/m}^3$ ,  
mass of the sphere of tissue under consideration =  $9.195 \times 10^{-5} \text{ Kg}$ .

Dose delivered to this mass =  $1.22 \times 10^{-9}$  Gray/positron.

The decay equation of figure 3-8 ( $y = 6759.9 e^{-0.005x}$ ) gives an estimate of 511 KeV photons detected from the positron decay. Each positron decay resulted in the emission of two 511 KeV photons. The detector detected 10% of what was emitted into  $4\pi$  steradians.

The estimated number of positrons released after the irradiation =  $33,800 \pm 411$  .

Total dose delivered in the sample of tissue by the recoil energy of positrons released in it =  $0.04 \pm 0.0005 \text{ mGy}$ .

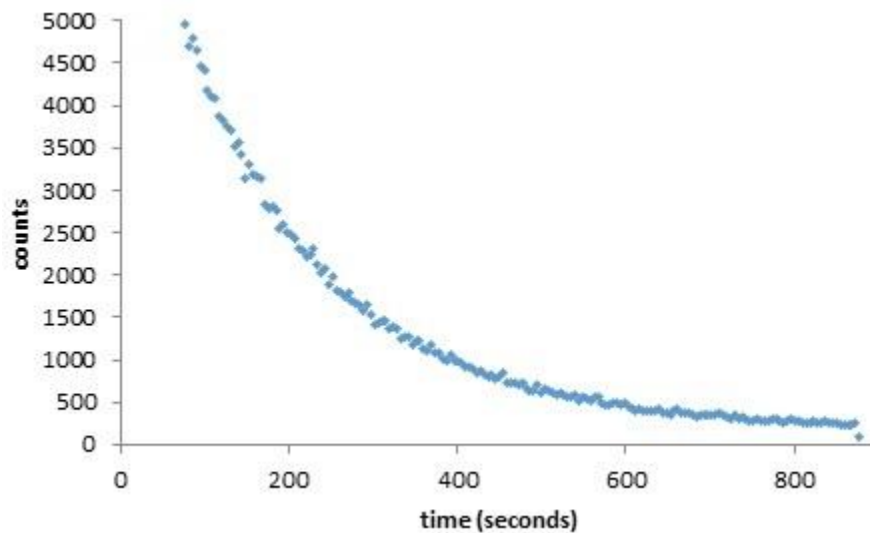


**Fig. 3-8.** Decay of activity from a sample of tissue irradiated by an 18 MV photon beam.

### Appendix 3

Order of magnitude calculation for the expected yield of positrons:

The bone was modelled as a cylinder of radius 0.6 cm and of length 15 cm. Taking the density of bone to be  $1900 \text{ Kg/m}^3$  and the density of marrow to be half the density of bone, the estimated number of oxygen atoms in this volume is of the order of  $10^{22}$ .

Using geometrical considerations, this volume can be reasonably approximated as the average of the volumes of the circumscribed and inscribed cuboids.

The reaction cross-section, as estimated from figure 3-11 and from the photon beam information provided by reference 45, is  $1.29 \times 10^{-29} \text{ cm}^2$  per atom per photon.

Considering a cube of bone of volume  $1 \text{ cm}^3$ , and assuming equal absorption in all the layers (given the small cross section), the cross section is of the order of  $10^{-7}$  per photon. Integrating this over the length of the cuboid, the cross section is of the order of  $10^{-6}$  per photon.

Taking the average energy of the 25 MV beam to be 8 MeV, the number of photons delivering 13 Gy is of the order of  $10^{10}$  to  $10^{11}$ .

This gives an estimated number of reactions in the order of  $10^5$  to  $10^6$ . So, the estimated number of positrons is of the order of  $10^5$  to  $10^6$  in magnitude.